Chemical Engineering Journal 526 (2025) 170526

Contents lists available at ScienceDirect

Chemical Engineering Journal

journal homepage: www.elsevier.com/locate/cej

# High-capacity and selective lithium-ion recovery via $Ti_3C_2T_x$@$SnO_2$ composite electrodes using hybrid capacitive deionization

Mohsen Askari [a], Andrea Merenda [a], Daksh Shah [b], Leonard Tijing [a], Ho Kyong Shon [a,*]

[a] ARC Research Hub for Nutrients in a Circular Economy, Centre for Technology in Water and Wastewater, School of Civil and Environmental Engineering, University of Technology Sydney, P. O. Box 123, 15 Broadway, NSW, 2007, Australia
[b] Applied Chemistry and Environmental Science, School of Science, STEM College, RMIT University, Melbourne, VIC, 3001, Australia

ARTICLE INFO

*Keywords:*
Lithium-ion recovery
Capacitive Deionization (CDI)
Ti3$C_2$Tx@$SnO_2$ electrode
Salt adsorption capacity (SAC)
Selectivity

ABSTRACT

The increasing demand for lithium in renewable energy storage has underscored the importance of developing sustainable and efficient recovery techniques, with hybrid capacitive deionization (HCDI) emerging as a promising approach through the use of advanced electrode materials. Herein, we outline the facile synthesis and comprehensive characterization of a $Ti_3C_2T_x$ MXene@$SnO_2$ composite electrode using SEM, TEM, XRD, FTIR, and XPS analyses to evaluate its performance in $Li^+$ ion adsorption compared to other monovalent metal ions ($K^+$ and $Na^+$). The structure–function relationship of the composite electrode was investigated, revealing that the incorporation of $SnO_2$ nanoparticles into $Ti_3C_2T_x$ MXene mitigates layer restacking, facilitates ion diffusion, and improves electrical conductivity. The influence of applied voltage and flow rate on lithium-ion transport dynamics was evaluated, revealing a salt adsorption capacity (SAC) of 191.7 $mg{\cdot}g^{-1}$ and an ASAR of 0.135 $mg{\cdot}g^{-1}{\cdot}s^{-1}$. In a ternary ion system, the electrode exhibited notable lithium selectivity, with ion removal efficiency ($\eta_M$) values of 42.4 %, 23.2 %, and 28.6 % for $Li^+$, $K^+$, and $Na^+$, respectively, and selectivity coefficients of $\rho_k^{Li} = 1.82$ and $\rho_{Na}^{Li} = 1.48$. The recovery studies highlighted a trade-off between high single-ion adsorption capacity and fast surface-driven kinetics of $Na^+$ and $K^+$, and the stronger, structurally anchored capture of $Li^+$ that dominants in competitive ternary system. Moreover, the electrode achieved a SAC of 103.4 $mg{\cdot}g^{-1}$ with an initial LiCl concentration set at 5 mM, and retained 82.7 % of this value after 20 adsorption–desorption cycles, demonstrating outstanding long-term cycling stability. These results highlight the $Ti_3C_2T_x$@$SnO_2$ composite as a highly efficient and durable electrode for lithium recovery, offering critical insights into the development of sustainable MXene-based energy storage and desalination technologies.

## 1. Introduction

Lithium, as a critical and largely irreplaceable element in clean energy technologies, plays a central role in reducing dependence on fossil fuels, with demand expected to grow consistently in the medium and long term [1–3]. To secure future lithium supplies, the recycling of Li-ion batteries, salty brines, and e-waste has gained increased prominence [4,5]. Additionally, cost-effective extraction methods from lithium-rich aqueous solutions have gained attention [6]. Accordingly, recent years have seen significant advancements in electrochemical techniques for Li recovery, including electrosorption and electrodialysis, which have led to the development of innovative electrode materials and membranes. These advancements offer significant advantages in lithium extraction, such as enhanced selectivity and improved recovery rates [7,8].

Among the emerging electrochemical processes, capacitive deionization (CDI) stands out as a superior ion removal technique, offering eco-friendliness and energy savings capabilities CDI is recognized as a selective ion capture method, characterized by a principal stack consisting of two parallel electrodes separated by a polymeric separator [9]. While conventional and modified CDI processes for Li recovery are relatively new —as reported by our group [10–12]—an emerging configuration called hybrid capacitive deionization (HCDI) is gaining attention. HCDI integrates porous carbon electrodes with pseudocapacitive electrodes, enabling ion storage within the electrode bulk rather than being confined to the surface, thus enhancing energy storage potential [13]. Additionally, the incorporation of faradaic materials in HCDI electrodes mitigates co-ion expulsion, a major limitation in CDI,

* Corresponding author.
*E-mail address:* hokyong.shon-1@uts.edu.au (H.K. Shon).

https://doi.org/10.1016/j.cej.2025.170526
Received 24 May 2025; Received in revised form 21 October 2025; Accepted 4 November 2025
Available online 7 November 2025

improving charge efficiency, capacity, and energy consumption [14]. While carbon-based electrodes exhibit limited capacities and their surface properties, electronic conductivity, and charge transport characteristics can adversely impact electrochemical performance [15], pseudocapacitive materials such as manganese oxide, titanium oxide, and vanadium oxide compounds have demonstrated improved performance due to their faradaic charge storage mechanisms [16,17].

To enhance the CDI-based lithium recovery performance, various asymmetric electrode configurations have been developed in which a $Li^+$ host electrode is paired with a complementary counter electrode. Yoon et al. [18] demonstrated an LMO‖Ag-AC system operated under stop-flow conditions, where the Ag-coated AC counter electrode enhanced the $Li^+$ adsorption capacity from 2.3 to 3.3 mg $g^{-1}$ and maintained 95 % of its initial capacity after 250 cycles at 10 mA $cm^{-2}$, confirming excellent cycling durability. Kim et al. [19]. reported a dual-ion battery-type configuration (LMO‖NTP), in which anion adsorption at the activated carbon electrode balanced the charge and enabled highly selective $Li^+$ recovery. The efficiency of lithium recovery exceeded 90 %, with over 96 % of the initial capacity retained after 50 cycles. More recently, a membrane-free HCDI system (LFP‖NVP) was introduced, in which NVP balanced the charge through $Na^+$ intercalation, achieving a cumulative $Li^+$ extraction rate of approximately 70 % after five consecutive cycles, indicating sustained performance [20]. However, the main focus has remained on developing novel materilas for the working electrodes of CDI-based systems, aiming to highlight improvements in Li recovery performance. In recent years, a range of ion-sieve materials—including lithium iron phosphate (LFP), lithium manganese oxide (LMO), lithium titanate (LTO), lithium nickel cobalt manganese oxide (LNCM), lithium–manganese–titanium oxide (LMTO), and lithium nickel manganese oxide (LNMO)—have been widely studied [7,21–23]. Their low cost, high theoretical specific capacity, and strong $Li^+$ selectivity [21] make them attractive candidates, yet their poor electrical conductivity and limited cycling stability remain significant challenges. To address these limitations, conductive additives have been incorporated, with approaches including the use of polypyrrole (PPy) in hybrid systems such as PSS/PPy copolymers [24] and reduced graphene oxide (3D-RGO) substrates for the in-situ growth of λ-$MnO_2$ [25]. These modifications have been shown to improve selectivity and accelerate equilibrium time [7]. Nevertheless, careful optimization of the amount of conductive material is essential, as excessive incorporation can reduce the number of active sites and thereby lower $Li^+$ adsorption capacity [26]. Recent studies have shown that MXene-based materials, owing to their high electrical conductivity ($2.4 \times 10^4$ S $Cm^{-1}$), combined with high capacitance, hydrophilicity, flexibility, and tunable surface chemistry, hold strong potential for enhancing $Li^+$ transport and selectivity in energy storage and ion separation technologies [27–29]. Srimuk et al. [30] pioneered the use of MXenes in CDI electrodes, which has since stimulated extensive development of MXene-based CDI materials [31–35]. Despite notable progress in desalination, the application of MXene electrodes in CDI for lithium recovery remains insufficiently explored.

The inherent layered structure of MXene electrodes often restricts efficient ion diffusion. To address this limitation, targeted engineering strategies have been developed to regulate and enlarge the interlayer spacing, thereby facilitating ion transport and reducing diffusion resistance. Among these approaches, composite modification has proven particularly effective [36]. Controlled regulation of the interlayer spacing is crucial not only to prevent irreversible restacking or agglomeration of nanosheets [33,37] but also to enhance electrolyte penetration, improve ion accessibility, and boost overall charge-storage performance [38]. Incorporating $SO_3H$-functionalized spacing agents into MXene structures has been shown to promote highly selective and rapid $Li^+$ transport within subnanochannels [39–41]. The MXene@PSS membrane demonstrates enhanced ion conductivity and superior $Li^+$ selectivity in mixed ionic environments, achieving $Li^+/Na^+$ and $Li^+/K^+$ selectivity ratios of 2.5 and 3.2, respectively [39]. Corresponding $Na^+$ and $K^+$ selectivity values were reported as 2.37 and 2.54, respectively. These findings highlight the potential of MXene-based structures for efficient $Li^+$ capture through CDI. Of the various composite engineering approaches applied to MXenes, integrating metal oxides (MOs) has emerged as a highly effective strategy for enhancing ion transport, enabling efficient intercalation, and maintaining a large specific surface area [27,37,42,43]. Among these metal oxides, tin dioxide ($SnO_2$) has gained particular attention due to its non-toxicity, affordability, high theoretical capacity, safe operating voltage, and chemical stability. Additionally, its effective intercalation capability helps prevent MXene restacking [44], thereby enhancing specific capacity without compromising mechanical integrity [45]. It was demonstrated that the layered structure of MXene ensures high conductivity and stability, forming an efficient framework for composite [44]. These MXene-based composites exhibited superior electrochemical performance, delivering reversible capacities of 635–1041 mAh $g^{-1}$, volumetric capacities up to 1375 mAh $cm^{-3}$, and capacity retentions above 94 % after 200 cycles, significantly outperforming pristine MXene and graphite electrodes [46,47]. They have also been widely investigated for LIB anodes [37,45], perovskite solar cells [48,49], supercapacitors [44], and gas sensors [45].

This study explores the development of composite $Ti_3C_2T_x$@$SnO_2$ electrodes for integration into HCDI systems, aiming to evaluate their efficiency in lithium-ion ($Li^+$) recovery in mixed ion solutions. To enhance $Li^+$ storage capacity, $SnO_2$ nanoparticles were incorporated into MXene nanosheets to improve ion accessibility and increase the availability of active sites. Additionally, the binder formulation was optimised to prevent blockage of these sites, thereby leveraging the multifunctional properties of MXene. A systematic investigation was carried out to thoroughly assess understanding of lithium-ion storage performance and ion transport efficiency, with particular emphasis on key operational parameters such as applied voltage and flow rate. Furthermore, the adsorption–desorption behaviour of $Li^+$ was examined and compared with other monovalent cations, including $K^+$ and $Na^+$, in multi-ion system. Finally, the long-term electrochemical stability of the composite electrode was assessed. A mechanistic analysis of the electrode performance is also presented, providing insights into the underlying interactions between the composite electrode material and $Li^+$ ions.

## 2. Experimental

### 2.1. Materials and reagents

MXene nanoflakes ($Ti_3C_2T_x$, 100–200 nm, Nanoshel), tin(IV) oxide (MW: 150.71 g/mol, Sigma-Aldrich), poly(vinylidene fluoride) (PVDF) powder (average MW ~530,000, pellets, Sigma-Aldrich), conductive carbon black (~30 nm, Nanografi), and commercially available porous electrodes (Siontech Co., Korea) fabricated using P-60 activated carbon (Kuraray Chemical Co., Japan) were employed in this study. 1-methyl-2-pyrrolidone (NMP) (Sigma-Aldrich), was utilized as the solvent. Reagent-grade lithium chloride (LiCl, MW: 42.39 g/mol, assay: >99 %), potassium chloride (KCl, MW: 74.55 g/mol, assay: >99 %), and sodium chloride (NaCl, MW: 58.44 g/mol, assay: >99 %), Obtained from Sigma-Aldrich and employed in feed solution preparation. Glass fiber prefilters (2 μm, Whatman) served as spacers in the CDI system, while all feed solutions were prepared using Milli-Q deionized water (18.2 MΩ·cm). All compounds were used as received without any further purification.

### 2.2. Preparation of the electrode

#### 2.2.1. Synthesis of $Ti_3C_2T_x$@ $SnO_2$

The $SnO_2$ nanoparticle solution (3 wt%) [48,50,51] was prepared and subjected to shaking for 15 min to form a stable $SnO_2$ colloidal solution. Simultaneously, 0.5 g of $Ti_3C_2T_x$ nanoflakes was dispersed in 100 mL of deionized (DI) water using a bath sonicator for 30 min, resulting in a uniform 5 mg.$mL^{-1}$ $Ti_3C_2T_x$ colloidal solution with well-dispersed

nanoflakes. The $Ti_3C_2T_x$colloidal solution was then gradually added dropwise to the $SnO_2$ colloidal solution under vigorous stirring for 6 h to ensure thorough mixing. The final $Ti_3C_2T_x$@$SnO_2$ composite was prepared at a weight ratio of 70:30 (MXene:$SnO_2$). The obtained $Ti_3C_2T_x$: $SnO_2$ composite dispersion was subsequently washed with DI water, filtered uisng a 0.22 μm filter, and vacuum-dried at 35 °C overnight. Finally, the dried material was collected and labelled as $Ti_3C_2T_x$@$SnO_2$ composite nanomaterial (see Fig. 1) [48,52].

#### 2.2.2. *Fabrication of $Ti_3C_2T_x$ @$SnO_2$ composite electrodes*

A schematic illustration of the synthesis of $Ti_3C_2T_x$@$SnO_2$ and electrode preparation is presented in Fig. 1. To prepare the electrodes, $Ti_3C_2T_x$@$SnO_2$ composite, conductive carbon black, and PVDF binder were dispersed in NMP to form a uniform slurry. The composition included 0.9 g of the adsorbent, 0.1 g of conductive carbon black, and an appropriate amount of PVDF solution. In contrast to the typical binder-to-adsorbent ratio of 1:10 used in electrode preparation, this study systematically examined lower PVDF loadings (1:100, 1:50, and 1:25) to minimize binder content while maintaining electrode integrity and performance. Experimental findings showed that the 1:100 and 1:50 ratios resulted in poor electrode adhesion and low packing density. In contrast, the 1:25 ratio produced a well-integrated electrode structure (Fig. S1), demonstrating strong adhesion and effective material distribution, and was therefore selected as the optimised ratio for electrode fabrication in all experiments. The slurry was then evenly cast onto a graphite sheet affixed to a motorized film applicator (Elcometer 4340) using double-sided Kapton tape. A 50 μm casting blade was employed to achieve a uniform film thickness. After an initial drying period of 10 min at ambient conditions, the electrodes were oven-dried at 50 °C overnight to ensure complete solvent evaporation and binder adhesion. The $Ti_3C_2T_x$ electrode was prepared using the same procedure [30,31].

### 2.3. *Material characterization*

The crystalline structure and phase composition of the powders and electrodes were analysed using X-ray diffraction (Bruker D8 Discover XRD, Bruker Corporation). The microstructure and morphology of the electrodes were examined using a scanning electron microscope (SEM, Zeiss Supra 55VP) and a transmission electron microscope (TEM, JEOL 2100F equipped with a Gatan One View camera). Microstructures and element distributions were detected under an energy dispersive spectrometer (EDS). TEM-EDS, and HR-TEM micrographs were acquired with an accelerating voltage of 200 keV. The samples were sonicated in isopropanol and dropped cast onto a carbon coated Cu grid. The samples were allowed to dry overnight at room temperature. The Fourier transform infrared (FT-IR) spectra of the composite electrodes were recorded using an IRPrestige-21 spectrometer (Shimadzu, Japan) across a wavenumber range of 400–4000 $cm^{-1}$ to identify functional groups, chemical bonds, and confirm the successful incorporation of materials. X-ray photoelectron spectroscopy (XPS) was performed using Thermoscientific K-alpha XPS with Al Kα (1486.7 eV). Pass energy was 50 eV, and an additional flood gun was used to flood analysis chamber with low energy $Ar^+$ and $e^-$. The take-off angle was 90°. The analysis chamber pressure was at $5 \times 10^{-8}$ Pa with beam spot size of 400 × 400 μm and energy step size of 0.02 eV. Each element was scanned 30 times for high resolution spectra, while survey spectra were scanned 5 times. Background used for correction was Shirley. Charge correction of the adventitious carbon peak was conducted at 284.8 eV. High-res valence band spectra were scanned 40 times, with energy step size 0.01 eV, and range −3 to 20 eV. To assess colloidal stability, zeta potential measurements of pristine $Ti_3C_2T_x$ and $Ti_3C_2T_x$@$SnO_2$ composite colloids at a concentration of 1 $mg.mL^{-1}$ in distilled water were performed using a Zetasizer Nano instrument (Nano ZS ZEN3600, Malvern Instruments, UK). All measurements were conducted at 25 °C, with each sample analysed three times, and the results expressed as mean zeta potential values. Finally, ion concentrations in effluent were measured using ICP-MS (Agilent 7900, Agilent Technologies, Inc.).

### 2.4. *Electrochemical measurements*

Electrochemical behaviour was evaluated by cyclic voltammetry (CV), galvanostatic charge–discharge (GCD), and electrochemical impedance spectroscopy (EIS) in 1 M LiCl aqueous electrolyte. Tests were performed on a CS350M potentiostat in a three-electrode cell configuration, both supplied by CorrTest, China.. $Ti_3C_2T_x$ and $Ti_3C_2T_x$@$SnO_2$ served as working electrodes, an Ag/AgCl electrode was the reference, and a platinum wire was the counter. CV was recorded from −1.0 to 0.4 V vs. Ag/AgCl at a scan rate of 5 mV $s^{-1}$. GCD profiles were collected in the same potential window at current densities of 1 A. $g^{-1}$. EIS was measured at open-circuit potential with a 5 mV sinusoidal perturbation over $10^5$ to 0.2 Hz, and the spectra were fitted with an equivalent circuit to obtain the relevant resistive and capacitive elements.

### 2.5. *Hybrid capacitive deionization (HCDI) test*

#### 2.5.1. *HCDI cell design*

The electrochemical performance of electrodes was evaluated using a HCDI system (Fig. 2). The experimental setup consisted of a CDI cell (The Electrode Store, TES), a peristaltic pump (GTS100, Green Tech, Korea), and a conductivity meter for continuous monitoring. A constant voltage was applied and precisely regulated using a potentiostat, the same electrochemical workstation for the electrochemical measurements. The HCDI cell was assembled using a pair of asymmetric

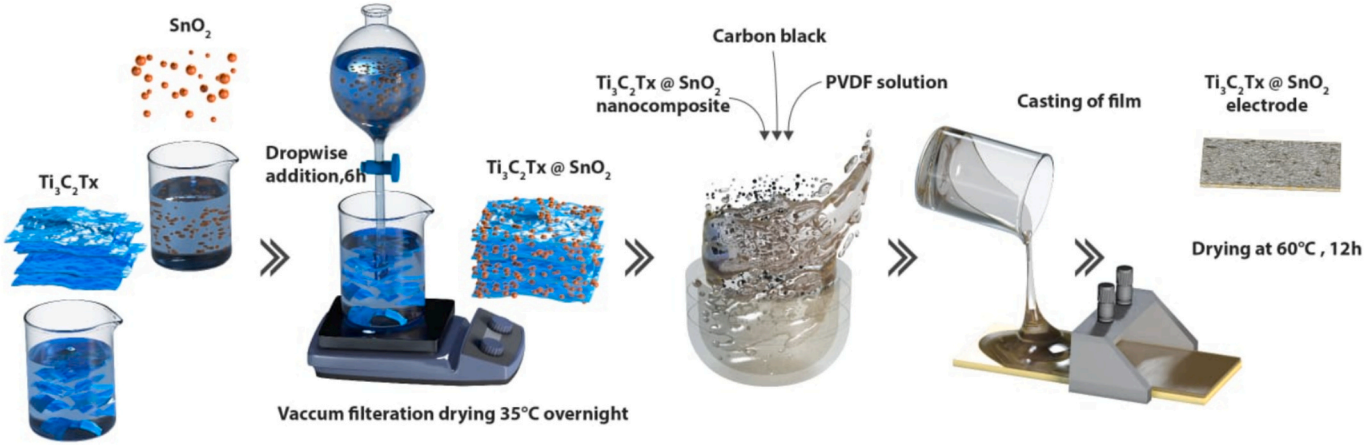


**Fig. 1.** Schematic illustration of the synthesis process of $Ti_3C_2T_x$@$SnO_2$ composite and electrode.

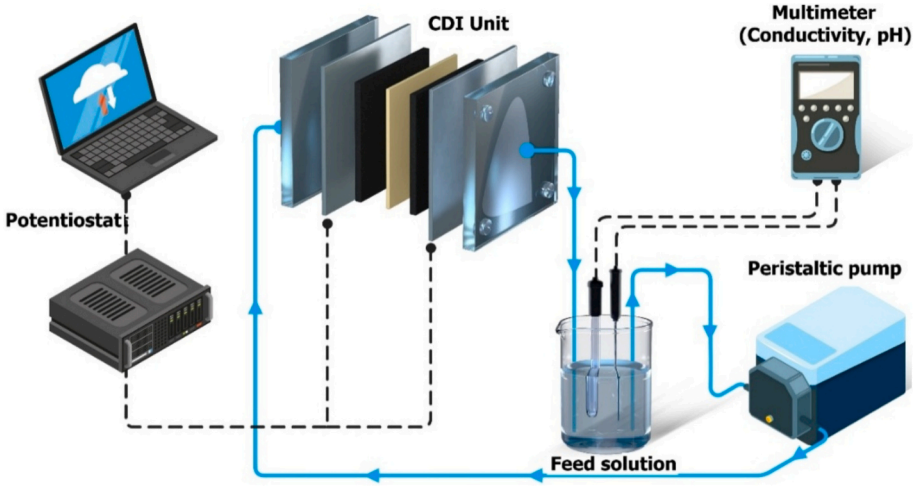


**Fig. 2.** Schematic representation of the experimental design.

electrodes, each with a geometric area of 2 × 2 $cm^2$. $Ti_3C_2T_x$@$SnO_2$ served as the cathode, while porous activated carbon was used as the anode. The cathode electrode was prepared with a mass loading of ~16 mg/$cm^2$ of active material. The electrodes were placed on either side of the current collector and firmly secured using acrylic end plates. A non-conductive spacer was placed between the electrodes to prevent short-circuiting and to ensure uniform fluid flow. This configuration is hereafter referred to as the $Ti_3C_2T_x$@$SnO_2$||AC cell. A schematic illustration of the HCDI unit is provided in Fig. S2. Electrical conductivity was monitored in real-time using a HACH HQ40d multi-meter in the feed reservoir, with data recorded at 10-s intervals.

### 2.5.2. HCDI electrosorption performance

The experimental tests were conducted in batch mode using a 200 mL feed solution containing 5 mM LiCl, which was introduced into the system. Prior to each experiment, the system was flushed with feed water to ensure uniform conductivity between the influent and effluent. To investigate ion transport dynamic through the composite electrode, electrosorption tests were conducted at cell voltages ranging from +0.8 V to +1.4 V (see Table S1), while maintaining a constant flow rate of 10 mL.$min^{-1}$. Additional tests were performed at flow rates of 3, 8, 13, and 18 mL.$min^{-1}$ under an optimised applied voltage to evaluate the impact of flow rate on system performance. For desorption studies, the adsorption-desorption behaviour of $Li^+$ was analysed and compared with $K^+$ and $Na^+$ under identical conditions. A single-component solution containing 5 mM of either LiCl, KCl, or NaCl was used, under the optimised flow rate and applied voltage. To minimize non-capacitive adsorption effects, a 10-min Milli-Q water washing phase—carried out without any electrode potential—was introduced before desorption. The desorption process was then performed by applying a voltage of opposite polarity. To assess the selectivity of $Li^+$ during electrosorption, tests were conducted using ternary mixtures containing lithium, potassium, and sodium ions. Stability tests were carried out over 20 cycles to evaluate long-term performance. Electrosorption tests were performed at 25 °C with 20-min adsorption and desorption cycles. Samples (1 mL each) were collected at 2-min intervals during electrosorption and 4-min intervals during desorption for further analysis. All experiments were performed in triplicate, and the mean values are reported.

The performance of the CDI cell was evaluated using key parameters, including salt adsorption capacity (SAC), salt desorption capacity (SDC), adsorption salt averagerate (ASAR), desprption salt average rate (DSAR), desorption efficiency (WD%), ion removal rate ($\eta_M$ %), and relative lithium selectivity ($\rho_M^{Li}$).

The SAC (mg.$g^{-1}$) and SDC (mg.$g^{-1}$) were determined using:

$$SAC = \frac{(C_{0,A} - C_{f,A}) \times V}{Wt\% \times M} \quad (1)$$

$$SDC = \frac{(C_{0,D} - C_{f,D}) \times V}{Wt\% \times M} \quad (2)$$

where $C_0$ and $C_f$ are the initial and final concentrations of the salt (mg.$L^{-1}$), respectively in adsorption(A) and desorption (D), $V$ is the volume of the feed solution (L), $Wt\%$ is the adsorbent content in the electrode (Wt%), and $M$ represents the active electrode mass (g);

The ASAR (mg.$g^{-1}$.$s^{-1}$) and DSAR (mg.$g^{-1}$.$s^{-1}$) were calculated as:

$$ASAR = \frac{SAC}{t_A} \quad (3)$$

$$DSAR = \frac{SDC}{t_D} \quad (4)$$

where, $t_A$ (s) and $t_D$ (s) represent adsorption and desorption times, respectively.

The desorption efficiency (WD%) was expressed as:

$$WD\ (\%) = \frac{SDC}{SAC} \times 100 \quad (5)$$

The ion removal efficiency ($\eta_M$)was given by:

$$\eta_M\ (\%) = 1 - \frac{C_t}{C_0} \quad (6)$$

where, $\eta_M$ (%) is represents the removal efficiency of cation $M$ (where M = Li, Na, or K), and $C_o$ and $C_t$ denote the concentrations of the cation at the initial time (0) and at time t, respectively.

Finaly, the relative selectivity of lithium ($\rho_M^{Li}$) was determined using:

$$\rho_M^{Li} = \left(\frac{C_0^{Li^+} - C_t^{Li^+}}{C_0^{Li^+}}\right) \div \left(\frac{C_0^{M^+} - C_t^{M^+}}{C_0^{M+}}\right) \quad (7)$$

where, $\rho_M^{Li}$ is denotes the relative selectivity of $Li^+$, while $C_o$ and $C_t$ represent the initial and time-dependent concentrations of the respective cations, respectively.

The energy demand of the process was quantified as the specific energy consumption (SEC), expressed in Wh.$mg^{-1}$ $Li^+$. The SEC was calculated by integrating the instantaneous electrical power during both the adsorption and desorption phases and normalizing to the amount of lithium recovered:

$$\mathrm{ESEC} = \frac{\int_0^{t_{ads}} U(t)I(t)dt + \int_0^{t_{des}} U(t)I(t)dt}{3600^{*}\eta_{Li}} \quad (8)$$

where $U$ is the cell voltage (V), $I$ is the applied current (A), $t_{ads}$ and $t_{des}$ are the durations of adsorption and desorption (s), respectively, and $\eta_{Li}$ is the number of moles of lithium recovered [53,54].

## 3. Results and discussions

### 3.1. Structure optimisation and characterization of the electrode

The fabrication process of the $Ti_3C_2T_x$@$SnO_2$ electrode is illustrated in Fig. 1. To enhance ion accessibility while preserving electrode performance, optimised PVDF concentrations were employed, as presented in Fig. S1. In contrast to the typical binder-to-adsorbent ratio of 1:10 used in electrode preparation, this study investigated lower PVDF concentrations (1:100, 1:50, and 1:25) to reduce binder content while preserving electrode performance. Experimental findings revealed that ratios below 1:25 compromised electrode adhesion and packing density. In contrast, the 1:25 ratio yielded a well-integrated electrode structure (Fig. S1), demonstrating strong adhesion and effective material distribution. Although the binder is essential for forming a cohesive structural network and enhancing material connectivity, excessive amounts can negatively impact performance by introducing insulating regions, obstructing ion pathways, and increasing ion transfer resistance [43,55]. Moreover, elevated binder content decreases surface conductivity, resulting in unstable current densities, an issue that is especially critical for the small-sized electrodes employed in this study [56]. The reduced PVDF content (Fig. S1b) in electrode fabrication is attributed to the multifunctional role of MXene. Beyond acting as an active adsorbent, MXene contributes to enhanced electrical conductivity, improved binder distribution [33], and effective interfacial bridging between $SnO_2$ nanoparticles and $Ti_3C_2T_x$ sheets.

SEM imaging was employed to examine the morphology of the materials. The characteristic accordion-like morphology of $Ti_3C_2T_x$, marked by voids between nanosheets resulting from van der Waals interactions, is presented in Fig. 3a [40,53]. The SEM image of $SnO_2$ nanoparticles reveals a relatively uniform size and well-dispersed morphology (Fig. 3b). SEM images of the $Ti_3C_2T_x$@$SnO_2$ and the corresponding electrode (Fig. 3.c and d) reveal that $SnO_2$ nanoparticles are firmly embedded within the $Ti_3C_2T_x$ nanosheet matrix, while the MXene retains its characteristic multi-layered structure. The intercalation of $SnO_2$ nanoparticles within MXene sheets enhances the structural connectivity of the electrode by expanding the interlayer spacing [54]. $SnO_2$ nanoparticles are also anchored onto the external surfaces of the MXene sheets. SEM–EDS elemental mapping and analysis of the $Ti_3C_2T_x$@$SnO_2$ composite (Fig. S3) confirm the presence of carbon and titanium (from MXene), as well as tin and oxygen (from $SnO_2$). Elemental mapping over a 25 μm region shows that nearly all particles exhibit co-localized Sn and Ti signals, indicating a high degree of intermixing between tin and titanium phases throughout the sample. These results are consistent with previous studies and confirm the successful synthesis of the $Ti_3C_2T_x$@$SnO_2$ composite [33,57,58].

The structural and elemental composition of nanocomposite electrodes with MXene and $SnO_2$ was analysed by TEM. The layered structure of MXene, the nanoparticle morphology of $SnO_2$, and their composite structure is shown in Fig. 4a-f. As shown in Fig. 4e and f $SnO_2$ nanoparticles are distributed along the length of the MXene sheets. Additionally, EDS analysis (Fig. 4g-k) confirms the uniform and widespread distribution of Sn, O, Ti, and C elements, validating the successful integration of $SnO_2$ and its effective interfacial contact with the MXene sheets. This layered architecture demonstrates a tightly bonded structure, which is critical for enhancing structural stability and electrochemical performance.

The structural characterization of the materials and composite is presented in Fig. 5a through XRD analysis. Distinct reflections of $SnO_2$ at approximately 27.1°, 34.1°, and 37.9°, corresponding to the (110), (101), and (200) crystal planes of tetragonal $SnO_2$, are evident in the composite. However, their reduced intensity compared to pure $SnO_2$ suggests that the $Ti_3C_2T_x$ matrix partially shields the diffraction from

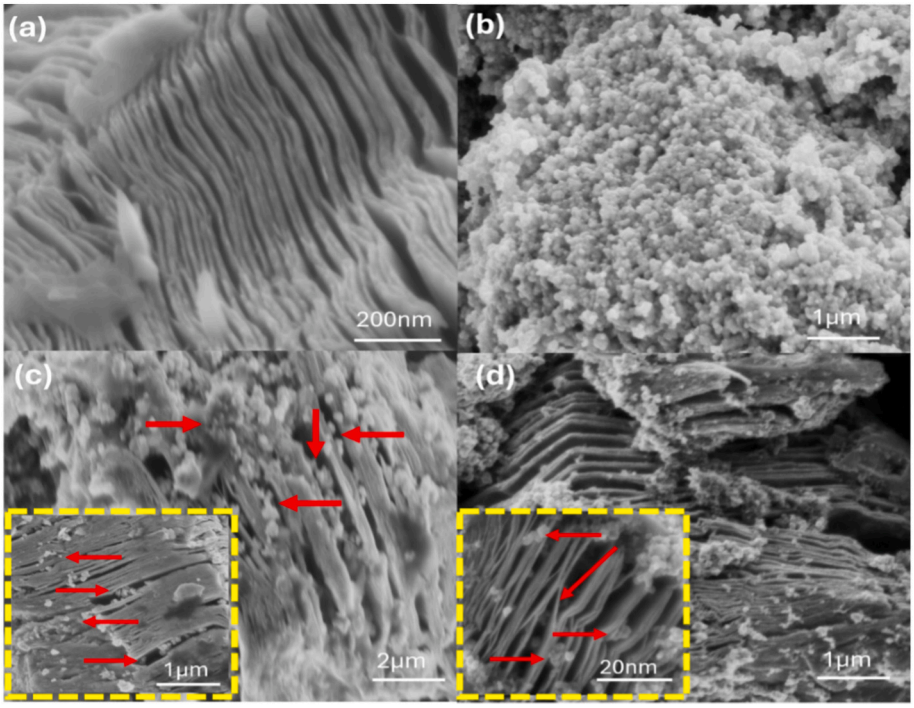


**Fig. 3.** SEM images of (a) $Ti_3C_2T_x$, (b) $SnO_2$, (c) $Ti_3C_2T_x$@SnO2 composite, and (d) $Ti_3C_2T_x$ @$SnO_2$ electrode. In panels (c) and (d), red arrows highlight the $SnO_2$ coating deposited both between the MXene layers (interlayer regions) and on their surfaces, indicating a well-distributed $SnO_2$ layer across the $Ti_3C_2T_x$ sheets. Insets in (c) and (d) provide magnified views of the lamellar MXene structure and the uniform $SnO_2$ integration.

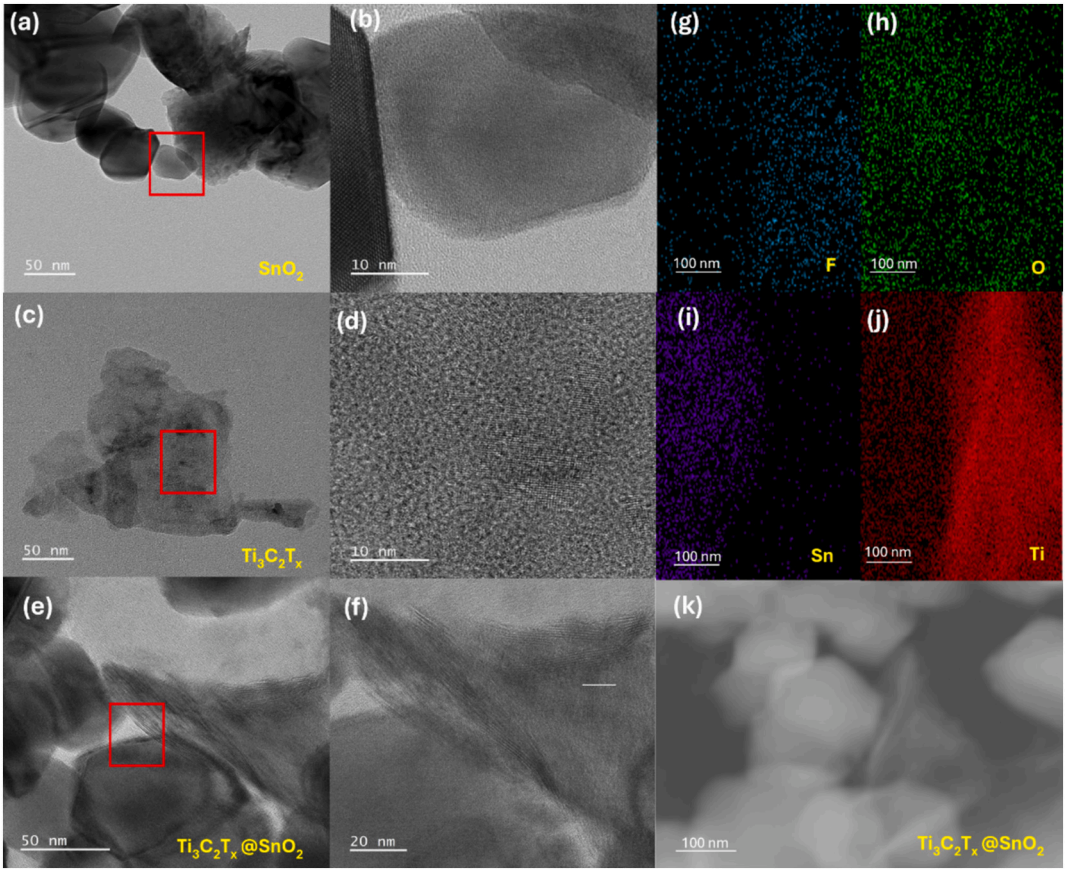


**Fig. 4.** (a) TEM image and (b) HRTEM image of $SnO_2$; (c) TEM image and (d) HRTEM image of $Ti_3C_2T_x$; (e) TEM image and (f) HRTEM image of the $Ti_3C_2T_x$@$SnO_2$ composite. Red squares in (a), (c), and (e) mark regions magnified in (b), (d), and (f), respectively; TEM-EDS maps of (g) F, (h) O, (i) Sn, and (j) Ti on the $Ti_3C_2T_x$@$SnO_2$ composite. (k) Corresponding TEM image.

$SnO_2$ crystallites [58]. Such reflection intensity variations and broadenings align with previous observations [52], indicating that the interaction between Sn-based nanostructures and MXene nanosheets can be attributed to the reduced crystallinity of $SnO_2$. The (002) reflection of $Ti_3C_2T_x$, observed around $2\theta = 9^\circ$, remains visible in the composite, indicating the retention of the MXene structure [59]. However, a slight shift and broadening of this reflection suggest an increase in interlayer spacing, likely due to the interaction between $SnO_2$ nanoparticles and $Ti_3C_2T_x$ sheets [33]. Furthermore, the disappearance or weakening of some higher-order $Ti_3C_2T_x$ reflections can be ascribed to the surface coverage of $Ti_3C_2T_x$ by $SnO_2$ [60], as shown in Fig. 3 c and d.

The chemical composition of the samples was evaluated using FTIR and XPS. As shown in the FTIR spectra of $Ti_3C_2T_x$, $SnO_2$, and $Ti_3C_2T_x$@$SnO_2$ materials (Fig. 5b), the spectra reveal characteristic structural and chemical features of each material. The $SnO_2$ spectrum features a broad 3400 $cm^{-1}$ band, attributed to adsorbed water, and a strong peak at ~600 $cm^{-1}$, corresponding to Sn—O—Sn stretching, indicative of its crystalline structure and phase purity. The $Ti_3C_2T_x$ spectrum exhibits a broad O—H stretching band near 3400 $cm^{-1}$, indicating its hydrophilic nature due to surface hydroxyl groups. Peaks in the 700–500 $cm^{-1}$ range correspond to metal–oxygen (M—O) bonds, which contribute to the structural stability and electronic properties of MXene. A weak peak near 620 $cm^{-1}$ arises from Ti—O deformation between Ti and surface —OH groups. In the $Ti_3C_2T_x$@$SnO_2$ composite, features from both components are present. The O—H stretching band at 3400 $cm^{-1}$ is slightly reduced, suggesting interactions between MXene and $SnO_2$ via hydrogen bonding or van der Waals forces. A peak at 1650 $cm^{-1}$ corresponds to C═O stretching, likely due to surface oxidation during etching and delamination. Enhanced peaks in the 700–500 $cm^{-1}$ region reflect contributions from MXene's M—O bonds and Sn—O—Sn structure, confirming the successful integration of $SnO_2$ into MXene [61–65].

XPS was conducted to analyse the surface compositions of materials and electrodes. As shown in Fig. 5c, the Ti 2p spectrum displays two characteristic broad peaks cantered at 455.6 eV and 462.0 eV, corresponding to the Ti—C bonds in $Ti_3C_2T_x$ (Ti $2p_{3/2}$ and Ti $2p_{1/2}$, respectively), confirming the presence of pristine MXene structure [58,66]. The broad nature of the Ti $2p_{3/2}$ in $Ti_3C_2T_x$ suggests the presence of Ti (III) and Ti(IV) oxidation states, indicating partial surface oxidation of $Ti_3C_2T_x$ to form $TiO_x$ species [37,60]. The presence of Ti (IV) states is further proved by the occurrence of Ti (IV) $2p_{3/2}$ peak at ~465 eV across all materials. The observed chemical shift in Ti binding energies for the $Ti_3C_2T_x$@$SnO_2$ composite and electrode samples is indicative of electronic interactions between the MXene surface and $SnO_2$ nanoparticles, suggesting the formation of a heterojunction. This phenomenon has been consistently reported in similar MXene–metal oxide nanohybrids, where interfacial coupling alters the electronic environment of Ti and facilitates charge transfer [66,67]. In Fig. 5d, the Sn 3d high-resolution XPS spectra of the composite exhibit two well-defined peaks at 486.4 eV (Sn $3d_{5/2}$) and 494.8 eV (Sn $3d_{3/2}$), which are attributed to $Sn^{4+}$ in $SnO_2$. These binding energies are consistent with standard tetravalent tin in $SnO_2$, as previously confirmed for $SnO_2$-modified MXene anodes [37,58,66]. For the electrode sample, a slight positive shift in Sn 3d peaks to 487.0 eV and 495.9 eV is observed, which is attributed to stronger electronic coupling between $SnO_2$ and $Ti_3C_2T_x$ [37]. This shift in binding energy reflects changes in the electronic environment of $Sn^{4+}$, indicating charge redistribution at the MXene/$SnO_2$ interface, a hallmark of heterojunction formation [67]. Furthermore, the progressive positive shift in the Sn 3d peaks from the composite (486.4/494.8 eV) to the electrode sample (487/495.9 eV) demonstrates a dynamic interfacial

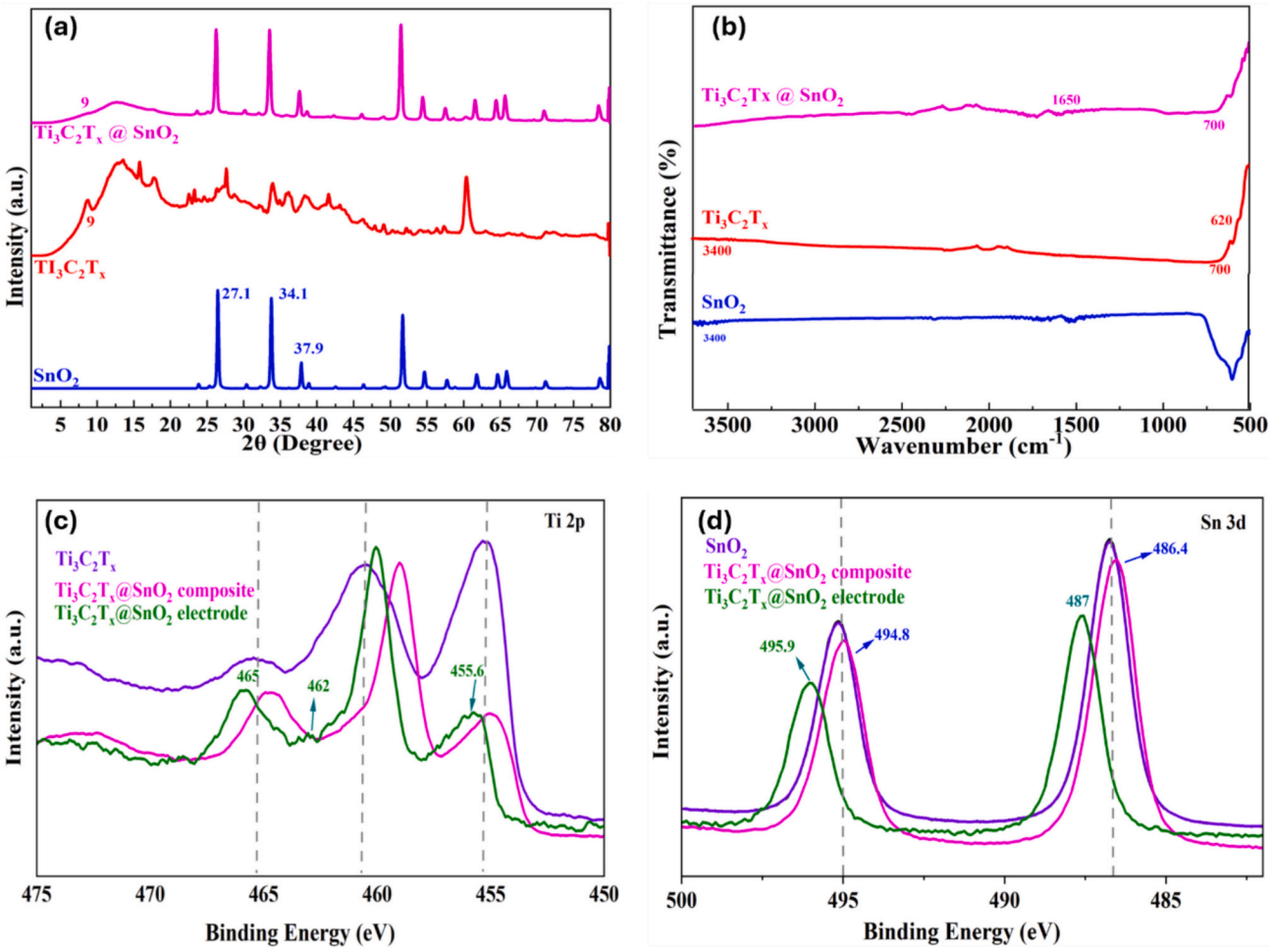


**Fig. 5.** (a) XRD patterns and (b) FTIR spectra of the $Ti_3C_2T_x$@$SnO_2$ composite; XPS spectra of (c) Ti 2p for $Ti_3C_2T_x$, $Ti_3C_2T_x$@$SnO_2$ composite, and $Ti_3C_2T_x$@$SnO_2$ electrode; (d) Sn 3d for $SnO_2$, $Ti_3C_2T_x$@$SnO_2$ composite, and $Ti_3C_2T_x$@$SnO_2$ electrode.

charge transfer, enhancing electronic coupling between $SnO_2$ and $Ti_3C_2T_x$ [58]. Such interfacial electron redistribution has been identified as a key mechanism for improved conductivity and $Li^+$ diffusion in MXene-based electrode materials [60,67]. These heterointerface are thus expected to facilitate efficient electron transport and reinforce electrochemical performance [37,66,67]. These findings collectively support the strong interfacial bonding between $Ti_3C_2T_x$ and SnO2, confirming the successful formation of the $Ti_3C_2T_x$@$SnO_2$ hybrid structure.

The zeta potential measurements revealed values of −25.2 mV for the $Ti_3C_2T_x$ solution, while the $Ti_3C_2T_x$@$SnO_2$ composite solution demonstrated a decrease in negative surface charge, with a zeta potential of −16.5 m*V*(Fig. 6a). The decreased zeta potential indicates that the surface of the $Ti_3C_2T_x$@$SnO_2$ composite is less negatively charged than that of pure $Ti_3C_2T_x$. This can be attributed to a reduction in resistance within the diffusion layer at the electrode-electrolyte interface, promoting more effective ion transfer to the electrode surface and reducing the co-ion repulsion effect, which may contribute to improved CDI performance [68].

The CV curves of the as-prepared $Ti_3C_2T_x$ and $Ti_3C_2T_x$@$SnO_2$ electrodes measured at 5 mV $s^{-1}$ are presented in Fig. 6b. Pristine $Ti_3C_2T_x$ exhibits a broad, feature-poor response, consistent with lower $Li^+$ storage capacity and the influence of surface functional terminations on ion transport in bare MXene [37,46]. In contrast, $Ti_3C_2T_x$@$SnO_2$ presents broad cathodic and anodic humps rather than distinct peaks; the larger loop area indicates greater pseudocapacitive contribution superposed on the capacitive background and a higher amount of reversible charge. This pattern agrees with MXene–$SnO_2$ studies that show quasi-rectangular CVs with small redox features and enlarged areas relative to bare MXene [44] and is consistent with prior reports on $Ti_3C_2T_x$ with Sn and on $SnO_2$@$Ti_3C_2T_x$ composites [37,46,69]. The strengthened faradaic response and cycling stability of the composite arise from introducing Sn-based species into $Ti_3C_2T_x$, which mitigates restacking, increases interlayer spacing, and provides conductive pathways and accessible active sites [37,69]. The GCD curves of MXene and MXene@$SnO_2$ at 1 A $g^{-1}$ within the potential range of −1.2 to 0.4 V vs Ag/AgCl are presented in Fig. 6c. Both profiles are quasi-triangular with small IR steps and mild curvature, which is typical of pseudocapacitive charge storage in MXene and $SnO_2$-based composites [70,71]. At the same current and ΔV the MXene@$SnO_2$ electrode exhibits a longer discharge time, indicating a higher apparent specific capacitance [1–4]. Its initial IR step is smaller than that of MXene, which indicates lower series resistance, increased electronic conductivity, and improved ion access, consistent with a MXene network that facilitates charge transport [70,72]. The composite trace is slightly more S-shaped, consistent with an added faradaic contribution from $SnO_2$ that supplies additional pseudocapacitance, while the charge and discharge branches remain close to mirror images, demonstrating good reversibility [70].

EIS was employed to evaluate charge transfer and mass transport. In $Ti_3C_2T_x$, the electrical conductivity is often superior to that of many other MXenes, contributing to favourable rate performance and cycle life [73]. According to the Nyquist plots (Fig. 6d), both electrodes display a depressed semicircle at high to mid frequencies, attributed to interfacial charge transfer, followed by a low-frequency tail

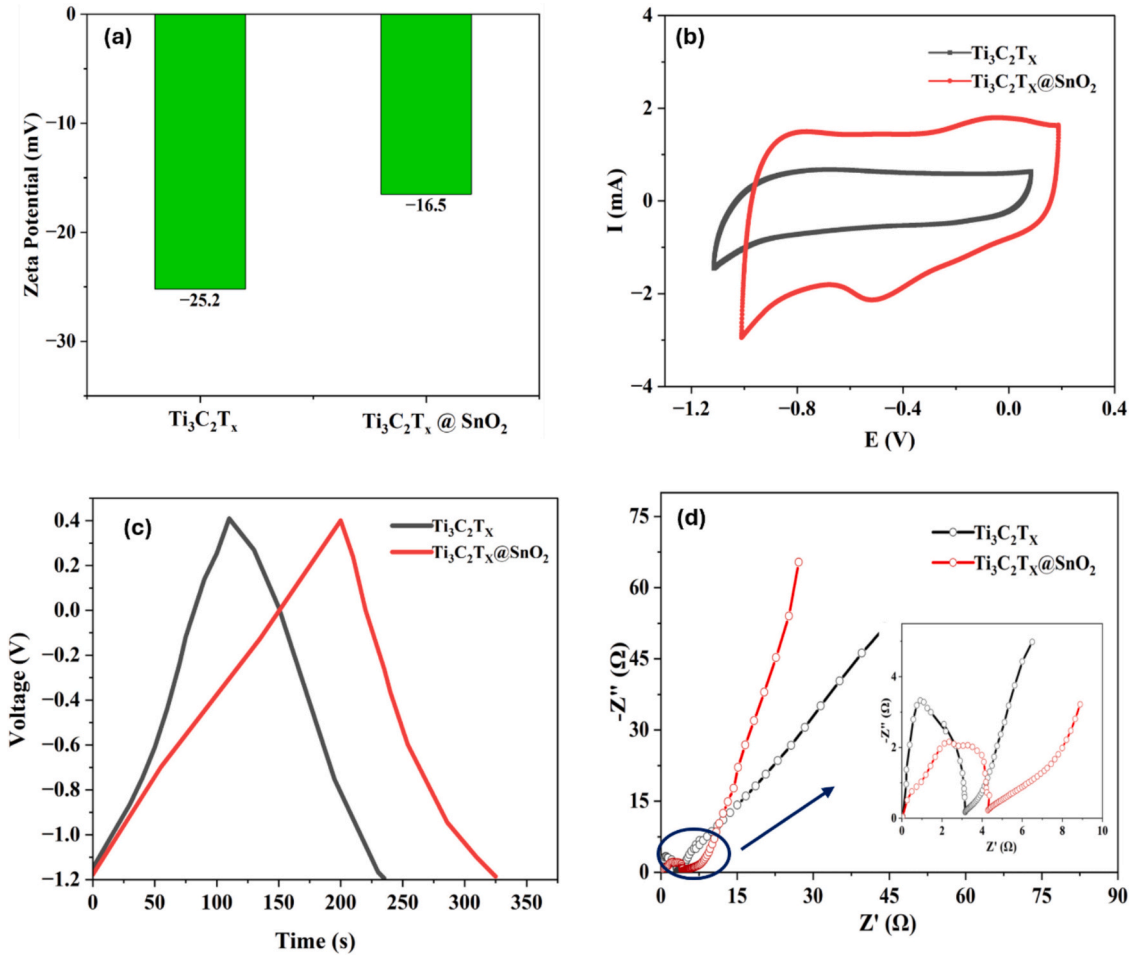


**Fig. 6.** (a) Zeta potential measurements of 1 mg $mL^{-1}$ dispersions at natural pH; (b) cyclic voltammograms (CV) recorded at 5 mV $s^{-1}$ within the potential window from −1.2 to 0.4 V; (c) galvanostatic charge–discharge (GCD) curves at 1 A $g^{-1}$; and (d) electrochemical impedance spectra (EIS, Nyquist plots) measured in 1 M LiCl over 100 kHz to 0.2 Hz with a 5 mV perturbation , all for $Ti_3C_2T_x$ and $Ti_3C_2T_x$@$SnO_2$.

characteristic of diffusion [37,46]. The spectra were fitted with a Randles circuit comprising $R_s$, $R_{ct}$, a constant-phase element (Q, n), and a finite-length Warburg element ($T_W$); the complete parameter sets are provided in Table S2. As summarised in Table S2, $Ti_3C_2T_x$@$SnO_2$ exhibits higher ohmic ($R_s$) and charge-transfer ($R_{ct}$) resistances, together with a larger and more non-ideal interfacial capacitance (Q, n) and a shorter diffusion timescale ($T_W$) relative to $Ti_3C_2T_x$, consistent with structure–transport relationships reported for related MXene systems [37,46,60,67,73]. This behaviour arises from $SnO_2$ nanoparticles anchored within the MXene framework (Fig. 5c, d), which form heterointerfaces that enhance electrolyte accessibility and ionic transport, thereby contributing to improved rate performance and stability.

### 3.2. *Investigation of ion transport dynamics*

The ion transport dynamics within the electrode was analysed by evaluating the influential operational parameters of the HCDI system, with a focus on the effects of applied voltage and flow rate. These two parameters serve as key indicators of ion transport characteristics, significantly impacting ion kinetics, thereby influencing the overall efficiency of ion transport within the electrode [55,74].

Since ion transport in nanochannels can be optimised by controlling surface charges [75], the lithium adsorption behaviour was evaluated at various cell voltages (0.8, 1.0, 1.2, and 1.4 V) while maintaining a constant flow rate of 10 mL.$min^{-1}$. As illustrated in Fig. S4a, for all applied voltages, conductivity initially dropped sharply, indicating rapid counterion adsorption onto the charged electrodes. As the system approached saturation, conductivity stabilized. Higher cell potentials led to greater overall conductivity reductions, confirming enhanced ion adsorption. The $Li^+$ adsorption capacities of the HCDI cell equipped with a $Ti_3C_2T_x$@$SnO_2$ cathode increased with applied voltage, measuring 47.7, 52.1, 64.4, and 90.1 mg.$g^{-1}$ at 0.8, 1.0, 1.2, and 1.4 *V*, respectively (Fig. 7a). The trend reflects the positive effect of higher voltage in promoting ion adsorption efficiency. The observed trend suggests that an increase in cell potential lowers the activation energy required for ion transport, facilitating the faster migration of $Li^+$ ions through MXene nanochannels. This aligns with the well-established principle that higher voltages generally reduce ion migration barriers, particularly in layered nanomaterials [76,77].

Additionally, ASAR analysis (see Table 1) indicates that at 0.8 V, the lowest voltage tested, both ASAR and SAC were at their minimum, with a consistent trend of improved ASAR as the voltage increased. Higher voltages effectively enhance ASAR by boosting ion mobility and adsorption rates, with peak ASAR values recorded at 1.4 V. At this voltage, the $Ti_3C_2T_x$@$SnO_2$ electrode exhibited its highest performance, achieving an ASAR of 0.077 mg·$g^{-1}$·$s^{-1}$ and a SAC of 90.5 mg.$g^{-1}$. The ASAR exhibits a pronounced increase in the 1.2–1.4 *V* range (Table 1), likely due to enhanced storage efficiency dominated by $Li^+$ intercalation at higher applied voltages. A similar trend has been reported in desalination experiments by Chen et al. [32]. These findings highlight the high performance of the $Ti_3C_2T_x$@$SnO_2$ electrode in $Li^+$ adsorption, which can be attributed to its layered structure, improved surface charge characteristics, and enhanced ion/electron transport, as discussed in Figs. 3d and 6d. These features significantly enhance ion transport

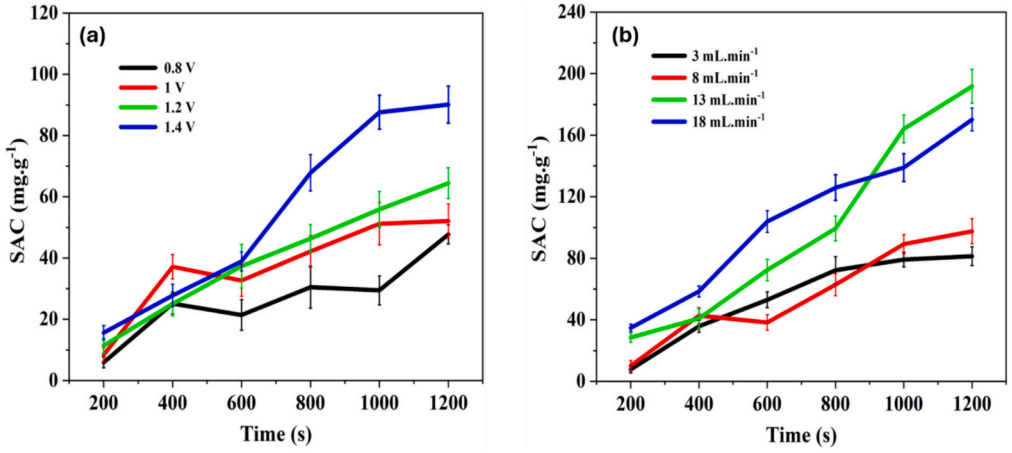


**Fig. 7.** Salt adsorption capacity (SAC) of $Ti_3C_2T_x$@$SnO_2$ electrodes over time in 5 mM LiCl solution at different (a) applied voltages (0.8, 1.0, 1.2, and 1.4 *V*) and (b) flow rates (3, 5, 8, and 13 mL.min$^{-1}$).

**Table 1**
Adsorption salt average rate (ASAR) of $Ti_3C_2T_x$@$SnO_2$ electrodes over time in 5 mM LiCl solution at different (a) applied voltages (0.8, 1.0, 1.2, and 1.4 V) and (b) flow rates (3, 5, 8, and 13 mL.min-1).

| | Applied voltage (v) | | | | Flow rate (mL.min$^{-1}$) | | | |
|---|---|---|---|---|---|---|---|---|
| | 0.8 | 0.1 | 1.2 | 1.4 | 3 | 8 | 13 | 18 |
| ASAR (mg·g$^{-1}$·s$^{-1}$) | 0.039 | 0.056 | 0.058 | 0.077 | 0.075 | 0.078 | 0.135 | 0.155 |

efficiency by extending the available nanochannel pathways, allowing more efficient ion movement through MXene nanochannels, surpassing the performance of conventional CDI materials [75]. As reported by studies on applied voltage effects in MXene-based electrodes [78,79], increasing the applied voltage enhances SAC and adsorption rate. These improvements are attributed to stronger Coulombic forces that accelerate ion migration, together with the intrinsic properties of wrinkle-engineered structures such as high conductivity, enlarged interlayer spacing, and abundant active sites that facilitate efficient ion transport [79]. Similarly, for MXene-based electrodes, 1.4 V Provided a balance of SAC, adsorption rate, and energy consumption in the $VS_2$/$V_2CTx$ hybrid electrode [78], and 1.6 V yielded the maximum SAC and fastest adsorption rate in wrinkle-engineered $Nb_4C_3Tx$ electrodes [79] (Additional findings on high-voltage effects are summarised in Table S1).

To assess the impact of flow rate on $Li^+$ adsorption, the performance of the $Ti_3C_2T_x$@$SnO_2$ cathode was further tested at 1.4 V in a 5 mM LiCl solution, using flow rates of 3, 8, 13, and 18 mL.min$^{-1}$, with SAC as the evaluation metric (Fig. 7b and Fig. S4b). The data indicate that increasing the flow rate enhances SAC, with a notable improvement at 13 mL.min$^{-1}$ across the entire time range, reaching approximately 191.7 mg.g$^{-1}$by 1200 s. In the initial 200 s, the SAC at 13 mL.min$^{-1}$ increases substantially, showing an approximate 300–400 % improvement compared to lower flow rates—28.4 mg.g$^{-1}$ at 13 mL.min$^{-1}$ versus 7.7 mg.g$^{-1}$ at 3 mL.min$^{-1}$ and 10.1 mg.g$^{-1}$at 8 mL.min$^{-1}$. This sharp increase suggests that ion transport limitations are more pronounced at lower flow rates. However, when the flow rate increases from 13 to 18 mL.min$^{-1}$, the incremental gain in SAC is minimal, indicating that 13 mL.min$^{-1}$ represents an optimal balance between ion transport efficiency and system operation. At moderate flow rates (8 and 13 mL.min$^{-1}$), SAC performance after the first 600 s becomes more stable. This stability likely reflects sufficient residence time, allowing ions to effectively migrate to and be adsorbed by the electrode. These findings contrast with conventional CDI systems, where increasing flow rates often lead to reduced SAC and ASAR values due to limited contact time between ions and electrodes [80]. As detailed in Table 1, a flow rate of 13 mL.min$^{-1}$ resulted in around 80% and 73% increase in ASAR compared to 3 and 8 mL.min$^{-1}$, demonstrating improved dynamic performance. However, at 18 mL.min$^{-1}$, the reduced residence time hinders ion-surface interaction, leading to rapid initial adsorption followed by a drop in efficiency as electrode saturation sets in. This underscores the importance of optimising flow rate to balance exposure time and ion transport [81]. While 18 mL.min$^{-1}$ offered a slightly higher initial SAC, a decline occurred around 1000 s, likely due to saturation effects. In contrast, 13 mL.min$^{-1}$ maintained a more consistent adsorption profile throughout the process. In this HCDI setup, increasing flow from 3 to 13 mL.min$^{-1}$ consistently improved performance, with SAC values of 81.4, 97.5, and 191.7 mg.g$^{-1}$at flow rates of 3, 8, and 13 mL.min$^{-1}$, respectively. At 18 mL.min$^{-1}$, however, SAC decreased slightly to 170.2 mg.g$^{-1}$. This improved performance at higher flow rates can be attributed to reduced boundary layer resistance, which enhances ion transport efficiency [82]. Overall, these findings underscore that, for the current device design and experimental parameters, 13 mL.min$^{-1}$ is the optimal flow rate, effectively balancing SAC and ASAR for the $Ti_3C_2T_x$@$SnO_2$ cathode in the HCDI system. This optimal rate aligns with literature on HCDI and redox flow battery systems, where higher flow rates enhance ion transport and increase SAC and ASAR by facilitating access to less accessible regions of the electrodes [83,84]. The relationship between transport dynamics and flow rate is governed by the corresponding flow regime [85]. At low flow (3 mL.min$^{-1}$), both SAC and ASAR are small, consistent with the dispersion-limited regime where ion supply is governed by diffusion and dispersion; in addition, during the early stage of charging salt adsorption is further restricted by low differential charge efficiency (ion swapping in micropores). As flow increases to 13 mL.min$^{-1}$, both SAC and ASAR rise, marking a transition into the advection-limited regime where advective transport enables more effective salt capture. At 18 mL.min$^{-1}$, SAC decreases while ASAR still increases; this can be explained by the fact that higher flow reduces the concentration drop per pass and thus lowers total capacity, while faster throughput boosts the average adsorption rate.

### 3.3. Ion recovery performance

#### 3.3.1. Desorption and selectivity

For desorption studies, an adsorption–desorption cycle was conducted for the $Ti_3C_2T_x$@$SnO_2$ electrode under a LiCl concentration of 5 mM, applying a potential of +1.4 *V* with a flow rate of 13 mL.min$^{-1}$ over a 20-min duration. To remove physiosorbed monovalent ions, a 10-min washing phase with Milli-Q water was introduced between the electrosorption and desorption phases. This washing step was conducted at zero applied potential (V = 0) and was performed just before initiating the desorption stage at −1.4 V. The same procedure was applied for 5 mM solutions of KCl and NaCl to compare the adsorption-desorption characteristics of these monovalent ions with those of $Li^+$ ions. The SAC, SDC, and WD efficiency values for each ion ($Li^+$, $K^+$, $Na^+$) were calculated using Eqs. (1), (2), and (5), and are shown in Fig. 8a.

In terms of SAC, the final values achieved for $Li^+$, $K^+$, and $Na^+$ were 106.1, 511.1, and 1372.8 mg.g$^{-1}$, respectively. The comparison of ions revealed higher SAC and ASAR values for $Na^+$ and $K^+$ compared to $Li^+$

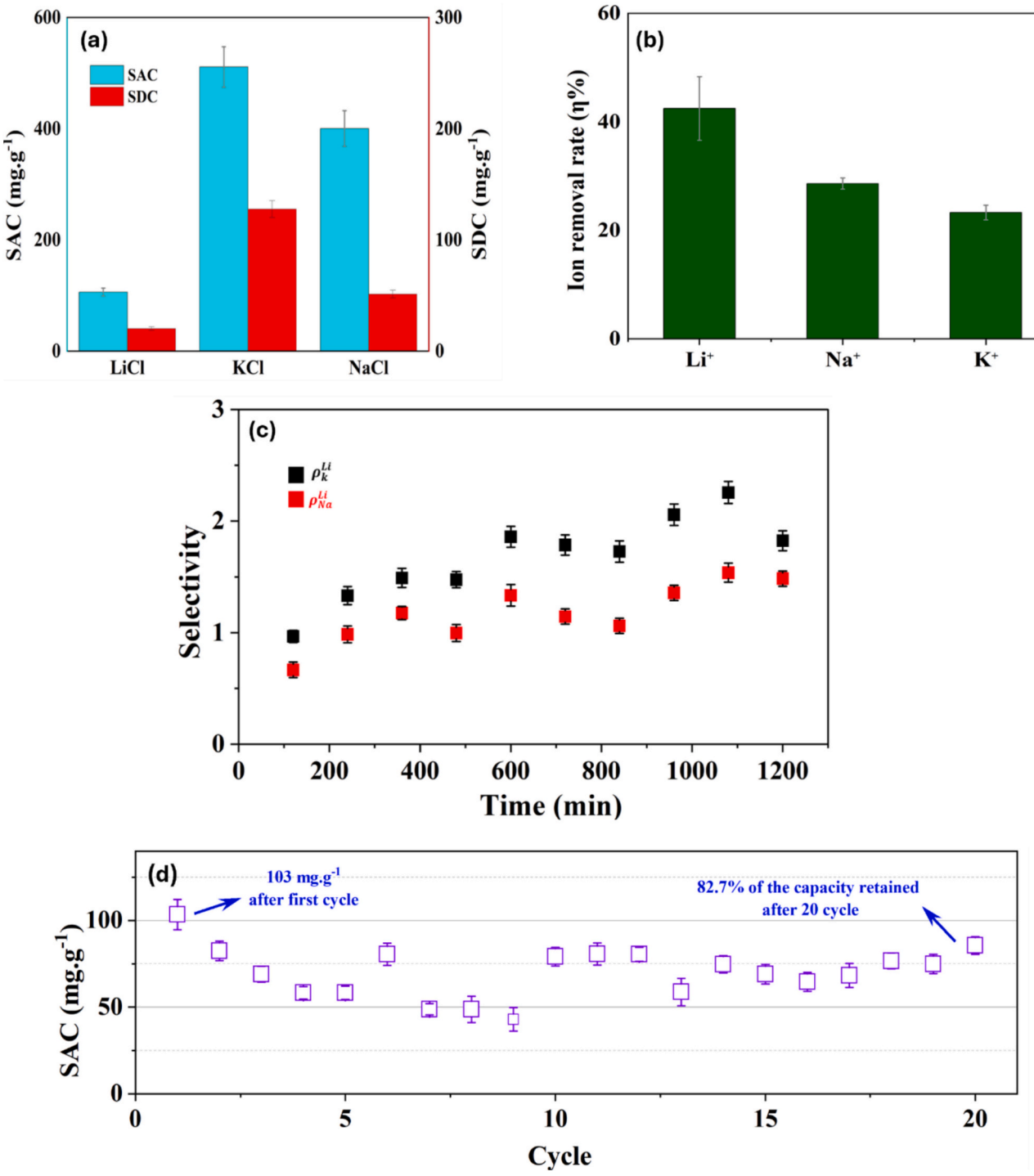


**Fig. 8.** (a) Salt adsorption capacity (SAC), salt desorption capacity (SDC), and desorption efficiency (WD%) for monovalent cations ($Li^+$, $Na^+$, $K^+$). (b, c) Lithium-ion selectivity in a ternary monovalent ion system ($Li^+$, $Na^+$, $K^+$): (b) selectivity coefficients of $Li^+$ over $Na^+$ and $K^+$, and (c) ion removal efficiency ($\eta_m$) for each ion. (d) Cyclic stability of the $Ti_3C_2T_x$@$SnO_2$ electrode over 30 electrosorption–desorption cycles using a LiCl solution at a concentration of 5 mM. All experiments were conducted at a flow rate of 13 mL.min$^{-1}$ and an applied voltage of 1.4 V.

($Na^+ > K^+ > Li^+$), with $Na^+$ and $K^+$ being adsorbed faster than $Li^+$, respectively. This trend is consistent with their lower hydration enthalpies (ΔH), which reduce the energy barrier for desolvation and facilitate faster ion transport (Table 2) [10]. $Na^+$ and $K^+$ have faster adsorption kinetics than $Li^+$, which favours rapid surface adsorption, whereas $Li^+$ uptake involves interlayer or structural incorporation. Notably, a significant portion of $K^+$ and $Na^+$ ions was removed during the washing phase (Fig. 8a, and Table S3), indicating that their adsorption is primarily surface-dominated and loosely bound. In contrast, $Li^+$ ions were likely intercalated into the $Ti_3C_2T_x$@$SnO_2$ structure. The desorption efficiency (WD) values were 19.03 % for $Li^+$, 24.99 % for $K^+$, and 12.79 % for $Na^+$, highlighting that $Na^+$ exhibited stronger surface retention despite its higher SAC. This indicates that $Na^+$, despite its higher SAC, was more strongly retained, likely due to moderate hydration energy and strong electrostatic interactions with the $Ti_3C_2T_x$@$SnO_2$ surface. This difference explains why $Na^+$ and $K^+$ outperform $Li^+$ in isolated systems but do not maintain the same advantage in mixed-ion conditions: their adsorption is high in capacity yet weakly bound, while $Li^+$, though slower to adsorb, forms more stable interactions within the electrode structure.

To evaluate selectivity, a ternary monovalent ion solution ($Li^+$, $K^+$, and $Na^+$) was prepared with initial feedwater concentrations of 5 mM for each salt. The feed volume was 200 mL, with a flow rate of 13 mL. $min^{-1}$, and an applied voltage of +1.4 V. The SAC of $Li^+$, $Na^+$, and $K^+$ ions was evaluated under these conditions using the $Ti_3C_2T_x$@$SnO_2$ electrode. The corresponding removal efficiency for each cation was measured and is presented in b and c. As shown in Fig. 8b, for the ternary solution, the $Ti_3C_2T_x$@$SnO_2$ electrode exhibited $\eta_M$ (%) values of 42.45 %, 23.27 %, and 28.61 % for $Li^+$, $K^+$, and $Na^+$, respectively, after 20 min of adsorption. Despite its lower SAC in single-ion systems, $Li^+$ displayed the highest removal efficiency in the competitive ternary environment, demonstrating preferential uptake. The relative selectivity ratios of $Li^+$ over $K^+$ and $Na^+$ ($\rho_k^{Li}$,and $\rho_{Na}^{Li}$) were 1.82 and 1.48, respectively. In comparison between single-ion SAC and mixed-ion selectivity, $Na^+$ and $K^+$ dominate in capacity under non-competitive conditions, whereas $Li^+$ is favoured in multicomponent systems due to its stronger structural incorporation and retention within the $Ti_3C_2T_x$@$SnO_2$ framework. This preferential adsorption of $Li^+$ can be attributed to the descending hydration enthalpies (ΔH: $K^+ < Na^+ < Li^+$) and hydrated radii (Hr) of the cations (Table 2) [10]. Ren et al. [88] similarly observed that for $Ti_3C_2T_x$ membranes, the permeation rate of $Li^+$ was found to be faster than that of $K^+$, suggesting the influence of specific ion-membrane interactions beyond hydration alone. Overall, these results illustrate a trade-off between high adsorption capacity, fast adsorption kinetics, and selective capture of monovalent ions. Table S.4 presents a comparison of reported MXene-based processes, highlighting the $Li^+$ selectivity of the MXene@$SnO_2$ CDI electrode. It should be noted that ion selectivity is highly system-dependent, strongly influenced by feedwater composition, and lacks standardized measurement protocols, making it not a universally comparable parameter, as emphasized in recent reviews [89–91].

### 3.3.2. Cyclic stability

To evaluate the regeneration performance of the Ti3C2Tx@$SnO_2$ electrode in HCDI for practical applications, its cyclic stability was assessed over 20 adsorption-desorption cycles using a LiCl solution, as shown in Fig. 8d. During each cycle, a significant decrease in solution conductivity was observed when a voltage of +1.4 *V* was applied, indicating ion adsorption. In contrast, switching the voltage to −1.4 V led to a sharp increase in conductivity, attributed to the release of ions from the electrodes back into the solution. The adsorption–desorption cycles exhibited an almost linear trend, with a slight decrease in salt adsorption capacity over time (Fig. 8d). Remarkably, the electrosorption capacity of lithium ions on the electrode after 20 cycles was 85.6 mg. $g^{-1}$, retaining 82.7 % of the initial value (103.4 mg.$g^{-1}$). This highlights the electrochemical reversibility of the cell in maintaining performance over multiple charge–discharge cycles. The stable charge–discharge cycling performance of the electrode indicates the incorporation of $SnO_2$ nanoparticles within the $Ti_3C_2T_x$ matrix, which contributes to preserving structural integrity over extended cycling periods cycling [92]. The comparison of the pristine $Ti_3C_2T_x$@$SnO_2$ electrode and the post-cycling electrode after 20 Li adsorption-desorption cycles was examined using XRD (Fig. S5) and SEM–EDS (Fig. S6). As shown in Fig. S5, t the primary diffraction peaks remain unchanged, with no significant peak shifts or ddditional reflections, indicating that the $Ti_3C_2T_x$@$SnO_2$ composite retains its crystalline structure throughout the cycling process. The absence of new diffraction peaks highlights the excellent structural stability of the material and supports its potential as a durable lectrode material for long-term CDI applications Complementary SEM–EDS analyses further illustrate this stability: the post-cycling electrode (Fig. S6) exhibits the same elemental distribution as the pristine composite (Fig. S3), with carbon and titanium from MXene together with tin and oxygen from $SnO_2$, thereby confirming the preservation of the composite's composition during repeated cycling.

Furthermore, the the $Ti_3C_2Tx$@$SnO_2$ electrode exhibits the highest reported SAC among CDI-based systems for lithium recovery from low-concentration feed solutions, to the best of on our knowledge, highlighting its exceptional potential as a highly efficient material for $Li^+$ adsorption. Table 3 summarizes the performance of the current electrode compared to selected previous reports in terms of lithium-ion adsorption capacity. During the 20-cycle stability test of $Li^+$ recovery at a cell voltage of 1.4 *V*, no gas formation was observed and pH variations remained negligible. These results confirm that water splitting did not occur and that the electrodes remained stable throughout cycling, consistent with previous CDI/HCDI studies conducted at higher voltages (up to 1.8 V) in desalination systems [32,93,94].

According to Eq. (8), the specific energy consumption (SEC) for lithium recovery during the first adsorption–desorption cycle was determined to be approximately 2.5 Wh $mol^{-1}$ $Li^+$. This value is comparable with those reported for many FCDI and MCDI systems. However, several optimised CDI and HCDI configurations have achieved lower SEC values [95–97]. While our system attains a high $Li^+$ adsorption capacity at this energy input, the SEC remains higher than the most energy-efficient CDI and the best-performing HCDI cases. Nevertheless, the performance is competitive with state-of-the-art CDI technologies and underscores the potential of the MXene-based HCDI system as an effective and sustainable approach for $Li^+$ extraction from brine resources.

### 3.3.3. Mechanism of $Li^+$ extraction

The high lithium-ion adsorption capacity of the $Ti_3C_2T_x$@$SnO_2$ electrode is attributed to its well-defined heterostructure, where $SnO_2$ is embedded within the MXene interlayer spacing and partially coated on its surface (Figs. 3c and d, 5c and d). This architecture effectively prevents MXene restacking, introduces additional active sites, and promotes uniform lithium-ion diffusion, thereby enhancing electrochemical performance. The synergy between the high electrical conductivity and lamellar structure of MXene and the semiconducting properties of $SnO_2$ facilitates strong interfacial contact [48,112], as also confirmed by the reduced IR drop in GCD (Fig. 6c) and the fitted EIS parameters (Fig. 6d). CV analysis (Fig. 6b) indicates that $SnO_2$ contributes to both

**Table 2**
Physical and hydration properties of different monovalent cations [10,75,86,87].

| Ion | Effective ionic diameter (Å) | Hydration diameter (Å) | Hydration free energy (kJ.$mol^{-1}$) | Hydration enthalpy (ΔH) | Charge density (Cd) |
|---|---|---|---|---|---|
| $Li^+$ | 2.12 | 7.64 | −498 | 519 | 49.05 |
| $K^+$ | 1.92 | 6.62 | −319 | 322 | 23.25 |
| $Na^+$ | 2.66 | 7.16 | −392 | 409 | 11.09 |

**Table 3**
Comparison of the investigated system with other materials under batch operation.

| System type | Electrode composition | LiCl concentration (mM) | Applied voltage (V) | SAC (mg.g$^{-1}$) | ASAR (mg.g$^{-1}$.s$^{-1}$) | Ref. |
|---|---|---|---|---|---|---|
| MCDI | rGO/$H_2TiO_3$-60 % ||Ac | 10 | 1.8 | 13.7 | 0.027 | [98] |
| MCDI | AC-PB20%|| Ac | 5 | 1.4 | 24.4 | 0.045 | [92] |
| MCDI | GO/La-LMO ||AC | 10 | – | 9.2 | 0.005 | [99] |
| MCDI | δ-$MnO_2$-x@CNTs || PC | 10 | 1.2 | 43.0 | 0.086 | [100] |
| HCDI | LMTO|| Ac | 15.7 | 2 | 4.7 | 0.026 | [101] |
| HCDI | Ni-MOF@CNT || Ac | – | 1.2 | 30.3 | 0.008 | [102] |
| HCDI | $Fe_3O_4$/N-doped carbon || Ac | 71.9 | 1.2 | 3.9 | 0.002 | [103] |
| HCDI | LMO-C|| Ac | 10 | 1.2 | 22.9 | 0.013 | [104] |
| HCDI | LMOns@CC|| Ac | 29.2 | 1.2 | 32.7 | 0.009 | [105] |
| HCDI | $AlF_3$-LMO|| Ac | 33.54 | 1.2 | 31.5 | 0.017 | [106] |
| HCDI | λ-$MnO_2$ nanorods||AC | 7.25 | 1.0 | 18.1 | 0.010 | [107] |
| HCDI | λ-$MnO_2$ || $LiMn_2O_4$ | 30 | 0.7 | 35 | 0.001 | [108] |
| HCDI | FO/NC500 ||AC | 11.6 | 1.2 | 28.9 | 0.010 | [93] |
| HCDI | LMO ||Ag-coated-AC | 10 | 1 | 3.3 | 0.0014 | [18] |
| HCDI | LMO/GO ||AC | 10 | 2.1 | 5.0 | 0.0037 | [109] |
| HCDI | LMO/LAO | 5 | 1.0 | 6.25 | 0.0037 | [110] |
| HCDI | LMO/$Li_3V_2(PO_4)_3$ | 4.72 | 1.2 | 19.1 | 0.0053 | [111] |
| HCDI | $Nb_4C_3T_x$ MXene || AC | 69.8 | 1.6 | 139.8 | 0.210 | [79] |
| HCDI | $Ti_3C_2T_x$ @$SnO_2$ || AC | 5 | 1.4 | 103.4 | 0.086 | This study |

pseudocapacitive behaviour, through surface-controlled redox reactions, and diffusion-controlled battery-type insertion. The enlarged CV loop area reflects fast surface pseudocapacitance, while the S-shaped features in GCD profiles (Fig. 6b) and the larger semicircle in EIS spectra (Fig. 6d) confirm the faradaic insertion of lithium at $SnO_2$ sites. This dual storage mechanism is consistent with prior reports on MXene–$SnO_2$ composites [37,69]. The faradaic process follows the reduction reaction [113]:

$$SnO_2 + 4Li^+ + 4e^- \rightarrow Sn + 2Li_2O \quad (9)$$

The formation of Sn—O—C bonds further enhances electron pathways and structural stability, reinforcing ion transport and electrode durability [113]. Minimizing binder content during fabrication further enhances conductive networks and ion transport. Together, these features explain thesuperior conductivity, enhanced lithium storage, and greater cycling stability of $Ti_3C_2T_x$@$SnO_2$ compared with bare MXene, while also mitigating particle aggregation [46,67,114].

At the interfacial level, the coherent MXene–$SnO_2$ heterojunctions facilitate efficient charge transfer and stabilise ion transport channels, supporting improved storage capacity and long-term performance. [115,116]. The interconnected MXene scaffold acts as a conductive backbone that stabilises $SnO_2$ nanoparticles against aggregation and maintains continuous electron/ion pathways. This robust network not only supports fast pseudocapacitive reactions but also enables faradaic conversion and alloying processes of $SnO_2$ with $Li^+$, representing a diffusion-controlled, battery-type contribution [37].

The high SAC and ASAR of monovalent cations in the $Ti_3C_2T_x$@$SnO_2$ electrode can be attributed to differences in their hydration sizes and hydration energies (Table 2). The single-layer $Ti_3C_2T_x$ nanosheet has a theoretical thickness of 8.8 Å, which increases the interlayer spacing. The hydration diameters of the cations follow the order: $Li^+$ (7.64 Å) > $Na^+$ (7.16 Å) > $K^+$ (6.62 Å). When these cations encounter nanochannels smaller than their hydration diameters, they undergo partial dehydration, reducing the number of coordinated water molecules to 2–3. This process decreases their effective sizes to approximately 3–4 Å, enabling the cations to pass through the electrode nanochannels with minimal resistance, thereby achieving higher SAC and ASAR [75]. The observed trend in hydration diameters ($K^+ < Na^+ < Li^+$) also correlates with the selective ion competition observed in ternary ion solutions. Furthermore, the relatively high capacitance density (Cd) of $Li^+$ (49.05C.mm$^{-3}$) played a pivotal role in its enhanced electrosorption, primarily driven by coulombic attraction [10]. This result also highlights $Li^+$ superior retention over extended periods, which can be attributed to its intercalation mechanism. As reported by Li et al. [117], the intercalation process significantly boosts the charge storage capability of $Ti_3C_2T_x$ as a result of the synergistic effects of optimised surface chemistry and improved ion diffusion pathways. Implementing an intercalation–deintercalation approach effectively expands the interlayer spacing, and upon cation extraction, a small proportion of cations remains confined within the interlayer voids. These residual cations function as structural stabilizers, preserving an open and accessible interlayer space, which in turn promotes efficient ion migration and storage. Moreover, the interaction between cations and —OH functional groups lead to the formation of surfaces enriched with —O terminations, which are particularly advantageous for redox reactions. These combined mechanisms offer a plausible explanation for the strong $Li^+$ adsorption performance over prolonged cycles, as intercalation greatly improves the long-term stability and durability of $Ti_3C_2T_x$@$SnO_2$.

## 4. Conclusions

This study developed a $Ti_3C_2T_x$@$SnO_2$ electrode as a high-performance material for lithium-ion recovery in HCDI systems. By addressing key challenges such as lamellar accumulation and limited ion separation in MXene-based materials, this rationally designed composite integrated $SnO_2$ while minimizing binder usage, resulting in superior structural and electrochemical properties. The $Ti_3C_2T_x$@$SnO_2$ composite demonstrated significantly improved performance particularly in lithium-ion capacity, ion transport efficiency, and cycling stability, due to its optimised material architecture. Key advancements included intercalated $SnO_2$, and additional active sites, and an increased conductivity, collectively facilitating efficient faradaic redox reactions, rapid $Li^+$ diffusion, and enhanced ion adsorption pathways. Further operational optimisation, particularly of the applied voltage and flow rate—enhanced ion transport dynamics, resulting in higher adsorption capacity, faster rates, and improved stability during adsorption–desorption cycles. Furthermore, ternary-mode desorption studies highlight its superior $Li^+$ adsorption over $K^+$ and $Na^+$ ions, with relative selectivity values of $\rho_k^{Li} = 1.82$ and $\rho_{Na}^{Li} = 1.48$ demonstrating its potential for efficient lithium recovery. The hybrid $Ti_3C_2T_x$@$SnO_2$||Ac cell exhibited an outstanding electrosorption capacity of 103.4 mg. g$^{-1}$, offering a significant advantage over previously reported materials. The performance of the $Ti_3C_2Tx$@$SnO_2$ composite remained stable, retained 82.7 % efficiency after 20 electrosorption-desorption cycles. These findings establish the $Ti_3C_2T_x$@$SnO_2$ electrode as an advanced solution that offers high capacity, fast kinetics, and long-term stability.

## CRediT authorship contribution statement

**Mohsen Askari:** Writing – original draft, Methodology, Investigation, Formal analysis, Data curation, Conceptualization. **Andrea Merenda:** Writing – review & editing, Investigation, Formal analysis, Data curation. **Daksh Shah:** Writing – original draft, Methodology, Investigation. **Leonard Tijing:** Writing – review & editing, Supervision, Formal analysis. **Ho Kyong Shon:** Writing – review & editing, Supervision, Resources, Project administration, Investigation, Funding acquisition, Formal analysis, Conceptualization.

## Declaration of competing interest

The authors declare that they have no known competing financial interests or personal relationships that could have appeared to influence the work reported in this paper.

## Acknowledgments

This research was supported by grants from the Australian Research Council (ARC) Discovery Projects (DP230100238). The authors acknowledge the facilities, and the scientific and technical assistance of the RMIT Microscopy & Microanalysis Facility (RMMF), a linked laboratory of Microscopy Australia.

## Appendix A. Supplementary data

Supplementary data to this article can be found online at https://doi.org/10.1016/j.cej.2025.170526.

## Data availability

Data will be made available on request.

## References

[1] J. Farahbakhsh, et al., Direct lithium extraction: a new paradigm for lithium production and resource utilization, Desalination 575 (2024) 117249.
[2] V. Balaram, et al., Lithium: a review of applications, occurrence, exploration, extraction, recycling, analysis, and environmental impact, Geosci. Front. 15 (5) (2024) 101868.
[3] M. Mura, et al., Global overview of the lithium market and opportunities for Chile, Resources 14 (2) (2025) 33.
[4] B. Swain, Recovery and recycling of lithium: a review, Sep. Purif. Technol. 172 (2017) 388–403.
[5] B.K. Pramanik, et al., Lithium recovery from salt-lake brine: impact of competing cations, pretreatment and preconcentration, Chemosphere 260 (2020) 127623.
[6] C.B. Tabelin, et al., Towards a low-carbon society: a review of lithium resource availability, challenges and innovations in mining, extraction and recycling, and future perspectives, Miner. Eng. 163 (2021) 106743.
[7] L. Wu, et al., Lithium recovery using electrochemical technologies: advances and challenges, Water Res. 221 (2022) 118822.
[8] P. Srimuk, et al., Charge-transfer materials for electrochemical water desalination, ion separation and the recovery of elements, Nat. Rev. Mater. 5 (7) (2020) 517–538.
[9] M. Askari, et al., Advances in capacitive deionization (CDI) systems for nutrient recovery from wastewater: Paving the path towards a circular economy, Desalination 583 (2024) 117695.
[10] S.M. Hossain, et al., ZiF-8 induced carbon electrodes for selective lithium recovery from aqueous feed water by employing capacitive deionization system, Desalination 546 (2023) 116201.
[11] H. Yu, et al., Selective lithium extraction from diluted binary solutions using metal-organic frameworks (MOF)-based membrane capacitive deionization (MCDI), Desalination 556 (2023) 116569.
[12] H. Yu, et al., Integrated sulfonated poly ether ketone membrane capacitive deionization for lithium recovery from diluted binary solutions, Sep. Purif. Technol. 352 (2025) 128064.
[13] M.E. Suss, V. Presser, Water desalination with energy storage electrode materials, Joule 2 (1) (2018) 10–15.
[14] E. Aytaç, et al., Faradaic deionization technology: insights from bibliometric, data mining and machine learning approaches, Desalination 563 (2023) 116715.
[15] W. Xi, et al., Hierarchical MXene/transition metal oxide heterostructures for rechargeable batteries, capacitors, and capacitive deionization, Nanoscale 14 (33) (2022) 11923–11944.
[16] Q. Li, et al., Faradaic electrodes open a new era for capacitive deionization, Adv. Sci. 7 (22) (2020).
[17] F. Yu, et al., Faradaic reactions in capacitive deionization for desalination and ion separation, J. Mater. Chem. A 7 (27) (2019) 15999–16027.
[18] H. Yoon, et al., Lithium-selective hybrid capacitive deionization system with a Ag-coated carbon electrode and stop-flow operation, Environ. Sci.: Water Res. Technol. 9 (2) (2023) 500–507.
[19] S. Kim, et al., Lithium recovery from brine using a λ-MnO2/activated carbon hybrid supercapacitor system, Chemosphere 125 (2015) 50–56.
[20] J. Zhang, et al., Membrane-free electrochemical extraction of lithium from geothermal water with transition metal ferrocyanide as a counter electrode, Appl. Energy 373 (2024) 123956.
[21] X. Shang, et al., LiNi0.5Mn1.5O4-based hybrid capacitive deionization for highly selective adsorption of lithium from brine, Sep. Purif. Technol. 258 (2021) 118009.
[22] H. Yu, et al., Highly selective lithium recovery from seawater desalination brine using $Li_2TiO_3$ membrane-coated capacitive deionization, Water Res. 285 (2025) 124113.
[23] A. Siekierka, Lithium and magnesium separation from brines by hybrid capacitive deionization, Desalination 527 (2022) 115569.
[24] X. Du, et al., A novel electroactive λ-MnO2/PPy/PSS core–shell nanorod coated electrode for selective recovery of lithium ions at low concentration, J. Mater. Chem. A 4 (36) (2016) 13989–13996.
[25] B. Hu, et al., Lithium ion sieve modified three-dimensional graphene electrode for selective extraction of lithium by capacitive deionization, J. Colloid Interface Sci. 612 (2022) 392–400.
[26] M. Liu, et al., A review on lithium extraction by electrochemical electrode deionization technology, J. Solid State Electrochem. 29 (5) (2025) 1577–1592.
[27] H. Younes, et al., Review on 2D MXene and graphene electrodes in capacitive deionization, Environ. Technol. Innov. 28 (2022) 102858.
[28] A. Shayesteh Zeraati, et al., Improved synthesis of Ti3C2Tx MXenes resulting in exceptional electrical conductivity, high synthesis yield, and enhanced capacitance, Nanoscale 13 (6) (2021) 3572–3580.
[29] K.R.G. Lim, et al., Fundamentals of MXene synthesis, Nat Synth 1 (8) (2022) 601–614.
[30] P. Srimuk, et al., MXene as a novel intercalation-type pseudocapacitive cathode and anode for capacitive deionization, J. Mater. Chem. A 4 (47) (2016) 18265–18271.
[31] S. Buczek, Rational design of titanium carbide mxene electrode architectures for hybrid capacitive deionization, Energy Environ. Mater. 3 (3) (2020) 398–404.
[32] Z. Chen, et al., Ti3C2 MXenes-derived NaTi2(PO4)3/MXene nanohybrid for fast and efficient hybrid capacitive deionization performance, Chem. Eng. J. 407 (2021) 127148.
[33] S. Wang, et al., Freestanding Ti3C2Tx MXene/prussian blue analogues films with superior ion uptake for efficient capacitive deionization by a dual pseudocapacitance effect, ACS Nano 16 (1) (2022) 1239–1249.
[34] L. Chen, et al., Carbon-incorporated Fe3O4 nanoflakes: high-performance faradaic materials for hybrid capacitive deionization and supercapacitors, Mater. Chem. Front. 5 (8) (2021) 3480–3488.
[35] S. Tian, X. Zhang, Z. Zhang, Capacitive deionization with MoS2/g-C3N4 electrodes, Desalination 479 (2020) 114348.
[36] S. Liu, et al., Functionalization strategies of MXene architectures for electrochemical energy storage applications, Energies 18 (5) (2025) 1223.
[37] H. Zhang, et al., 3D d-Ti3C2 xerogel framework decorated with core-shell SnO2@C for high-performance lithium-ion batteries, Electrochim. Acta 285 (2018) 94–102.
[38] Y. Li, S. Vallem, J. Bae, MXene-based composites for high-performance and fire-safe lithium-ion battery, Curr. Appl. Phys. 53 (2023) 142–164.
[39] X. Tong, et al., MXene composite membranes with enhanced ion transport and regulated ion selectivity, Environ. Sci. Technol. 56 (12) (2022) 8964–8974.
[40] Y. Huang, et al., MXene-coated ion-selective electrode sensors for highly stable and selective lithium dynamics monitoring, Environ. Sci. Technol. 58 (2) (2024) 1359–1368.
[41] Z. Lu, et al., A lamellar MXene (TiCT)/PSS composite membrane for fast and selective lithium-ion separation, Angew. Chem. Int. Ed. 60 (41) (2021) 22265–22269.
[42] M. Boota, Pseudocapacitive electrodes produced by oxidant-free polymerization of pyrrole between the layers of 2D titanium carbide (MXene), Adv. Mater. 28 (7) (2015) 1517–1522.
[43] X. Qiang, et al., Boosting the lithium storage of tin dioxide nanotubes by MXene inks as conductive binder, Chem. Lett. 51 (6) (2022) 585–589.
[44] N. Prabhakar, et al., Influence on effective and ineffective delamination of MXene (Ti3C2Tx) by tightly anchoring tin oxide nanocomposite for boosting the specific capacitance of supercapacitor, J. Alloys Compd. 921 (2022) 166092.
[45] A. Gentile, et al., Unraveling the electrochemical mechanism in tin oxide/MXene nanocomposites as highly reversible negative electrodes for lithium-ion batteries, Adv. Mater. Interfaces 10 (12) (2023).
[46] B. Ahmed, et al., Atomic layer deposition of SnO2 on MXene for Li-ion battery anodes, Nano Energy 34 (2017) 249–256.
[47] J. Luo, et al., Sn4+ ion decorated highly conductive Ti3C2 MXene: promising lithium-ion anodes with enhanced volumetric capacity and cyclic performance, ACS Nano 10 (2) (2016) 2491–2499.
[48] M.F.U. Din, et al., Tailoring the electronic properties of the SnO2 nanoparticle layer for n-i-p perovskite solar cells by Ti3C2TX MXene, Mater Today Commun 36 (2023) 106700.

[49] H. Zheng, et al., Controlling the defect density of perovskite films by MXene/SnO2 hybrid electron transport layers for efficient and stable photovoltaics, J. Phys. Chem. C 125 (28) (2021) 15210–15222.
[50] L. Yang, et al., SnO2–Ti3C2 MXene electron transport layers for perovskite solar cells, J. Mater. Chem. A 7 (10) (2019) 5635–5642.
[51] L. Yin, et al., Functionalized-MXene-nanosheet-doped tin oxide enhances the electrical properties in perovskite solar cells, Cell Reports Phys. Sci. 3 (6) (2022) 100905.
[52] Z. Wang, et al., Synthesis of three-dimensional Sn@Ti3C2 by layer-by-layer self-assembly for high-performance lithium-ion storage, J. Colloid Interface Sci. 577 (2020) 329–336.
[53] Y. Xiong, et al., Electrochemical lithium extraction from aqueous sources, Matter 5 (6) (2022) 1760–1791.
[54] D.-H. Lee, et al., Selective lithium recovery from aqueous solution using a modified membrane capacitive deionization system, Hydrometallurgy 173 (2017) 283–288.
[55] Y. Cai, et al., Maximized ion accessibility in the binder-free layer-by-layer MXene/CNT film prepared by the electrophoretic deposition for rapid hybrid capacitive deionization, Sep. Purif. Technol. 292 (2022) 121019.
[56] M.-I. Jamesh, Recent advances on flexible electrodes for Na-ion batteries and Li–S batteries, J. Energy Chem. 32 (2019) 15–44.
[57] X. Shen, et al., All-MXene-based integrated membrane electrode constructed using Ti3C2Tx as an intercalating agent for high-performance desalination, Environ. Sci. Technol. 54 (7) (2020) 4554–4563.
[58] Z. Wang, et al., SnO-SnO2 modified two-dimensional MXene Ti3C2Tx for acetone gas sensor working at room temperature, J. Mater. Sci. Technol. 73 (2021) 128–138.
[59] M. Torkamanzadeh, et al., MXene/activated-carbon hybrid capacitive deionization for permselective ion removal at low and high salinity, ACS Appl. Mater. Interfaces 12 (23) (2020) 26013–26025.
[60] J. Ai, et al., SnS nanoparticles anchored on Ti3C2 nanosheets matrix via electrostatic attraction method as novel anode for lithium ion batteries, Chem. Eng. J. 357 (2019) 150–158.
[61] Y.-U. Haq, et al., Synthesis and characterization of 2D MXene: device fabrication for humidity sensing, J. Sci. Adv. Mater. Dev. 7 (1) (2022) 100390.
[62] X. Huang, W. Mu, C. Chang, Two-dimensional Ti3C2 MXene-derived Ti3C2-Ti2C-TiO2 materials for improved diclofenac sodium adsorption performance, Environ. Sci. Pollut. Res. 30 (18) (2023) 52157–52168.
[63] M. Akram, et al., Continuous microwave flow synthesis (CMFS) of nano-sized tin oxide: effect of precursor concentration, Ceram. Int. 42 (7) (2016) 8613–8619.
[64] M. Javed, et al., Fabrication of effective Co-SnO2/SGCN photocatalysts for the removal of organic pollutants and pathogen inactivation, Crystals 13 (2) (2023) 163.
[65] P.A. Luque, et al., SnO2 nanoparticles synthesized with citrus aurantifolia and their performance in photocatalysis, J. Mater. Sci. Mater. Electron. 31 (19) (2020) 16859–16866.
[66] T. He, et al., MXene/SnO2 heterojunction based chemical gas sensors, Sensors Actuators B Chem. 329 (2021) 129275.
[67] J. Xiong, et al., Synergistically enhanced lithium storage performance based on titanium carbide nanosheets (MXene) backbone and SnO2 quantum dots, Electrochim. Acta 268 (2018) 503–511.
[68] S. Xu, et al., The effect of crystal phase of manganese oxide on the capacitive deionization of simple electrolytes, Sci. Total Environ. 675 (2019) 31–40.
[69] S. Zhang, et al., Partial atomic tin nanocomplex pillared few-layered Ti3C2Tx MXenes for superior lithium-ion storage, Nano-Micro Lett. 12 (1) (2020) 78.
[70] H. Osora, et al., Hydrothermally grown SnO2 and SnO2/rGO nanocomposite and its physio-electrochemical studies for pseudocapacitor electrode applications, J. Clust. Sci. 35 (3) (2024) 891–901.
[71] R.A. Murugesan, K.C. Nagamuthu Raja, Capacitance performance of Ti3C2Tx MXene nanosheets on alkaline and neutral electrolytes, Mater. Res. Bull. 163 (2023) 112217.
[72] A. Padhy, et al., A SnO2/MXene hybrid nanocomposite as a negative electrode material for asymmetric supercapacitors, Sustainable Energy Fuels 7 (21) (2023) 5271–5282.
[73] R. Ma, et al., Self-supporting, binder-free, and flexible Ti3C2Tx MXene-based supercapacitor electrode with improved electrochemical performance, ACS Nano 16 (6) (2022) 9713–9727.
[74] C. Liu, et al., Application of capacitive deionizing membrane distillation (CDIMD) system for seawater desalination: emphasizing on the impacts of operating parameters, Desalination 567 (2023) 116998.
[75] M. He, et al., Carboxymethylcellulose (CMC)/glutaraldehyde (GA)-modified Ti3C2Tx membrane and its efficient ion sieving performance, J. Membr. Sci. 675 (2023) 121541.
[76] D. Liu, et al., Electrochemical system with LiMn2O4 porous electrode for lithium recovery and its kinetics, Sep. Purif. Technol. 270 (2021) 118809.
[77] J. de Rojas, et al., Voltage-driven motion of nitrogen ions: a new paradigm for magneto-ionics, Nat. Commun. 11 (1) (2020) 5871.
[78] F. Yu, et al., V2CTx-MXene partially derived hybrid VS2/V2CTx electrode for capacitive deionization with exceptional rate and capacity, J. Mater. Chem. A 10 (44) (2022) 23531–23541.
[79] H. Liu, et al., Capacitive deionization using wrinkle-engineered Nb4C3Tx-MXene freestanding membranes, Chem. Eng. J. 507 (2025) 160441.
[80] M. Mossad, L. Zou, A study of the capacitive deionisation performance under various operational conditions, J. Hazard. Mater. 213-214 (2012) 491–497.
[81] K. Dehghan, S.A. Mirbagheri, M. Alam, Investigation of Effective Parameters on Brackish Water Desalination by Flow-Electrode Capacitive Deionization, Preprints, 2021. Preprints.
[82] Ö. Tekinalp, et al., Cation exchange membranes and process optimizations in electrodialysis for selective metal separation: a review, Membranes 13 (2023), https://doi.org/10.3390/membranes13060566.
[83] L. Agartan, et al., Influence of operating conditions and cathode parameters on desalination performance of hybrid CDI systems, Desalination 452 (2019) 1–8.
[84] C.R. Dennison, et al., Enhancing mass transport in redox flow batteries by tailoring flow field and electrode design, J. Electrochem. Soc. 163 (1) (2016) A5163.
[85] Y. Qu, et al., Charging and transport dynamics of a flow-through electrode capacitive deionization system, J. Phys. Chem. B 122 (1) (2018) 240–249.
[86] H.D.B. Jenkins, M.S.F. Pritchett, A new approach to the analysis of absolute free energies, enthalpies and entropies of hydration of individual gaseous ions and absolute single-ion viscosity B-coefficients, J. Chem. Soc. Faraday Trans. 80 (1984) 721–737.
[87] K.D. Collins, Sticky ions in biological systems, Proc. Natl. Acad. Sci. USA 92 (12) (1995) 5553–5557.
[88] C.E. Ren, et al., Charge- and size-selective ion sieving through Ti3C2Tx MXene membranes, J. Phys. Chem. Lett. 6 (20) (2015) 4026–4031.
[89] M.E. Suss, et al., Water desalination via capacitive deionization: what is it and what can we expect from it? Energy Environ. Sci. 8 (8) (2015) 2296–2319.
[90] S.A. Hawks, et al., Performance metrics for the objective assessment of capacitive deionization systems, Water Res. 152 (2019) 126–137.
[91] T. Pang, et al., Advances and challenges in capacitive deionization: materials, architectures, and selective ion removal, Desalination 592 (2024) 118140.
[92] M. Rethinasabapathy, et al., Efficient lithium extraction using redox-active prussian blue nanoparticles-anchored activated carbon intercalation electrodes via membrane capacitive deionization, Chemosphere 336 (2023) 139256.
[93] G. Zhang, et al., Freestanding N-doped graphene membrane electrode with interconnected porous architecture for efficient capacitive deionization, Carbon 187 (2022) 86–96.
[94] S. Liu, et al., Metal-organic framework–derived carbon/N-doped three-dimensional reduced graphene oxide composite with high capacitive deionization performance, Mater. Today Sustain. 20 (2022) 100228.
[95] D. Jiang, et al., Insights into electrochemical paradigms for lithium extraction: electrodialysis versus capacitive deionization, Coord. Chem. Rev. 516 (2024) 215923.
[96] A. Siekierka, M. Bryjak, Selective sorbents for recovery of lithium ions by hybrid capacitive deionization, Desalination 520 (2021) 115324.
[97] W.A. El-Fattah, et al., Electrochemical lithium extraction from desalination brine via lithium-manganese oxide intercalation electrodes in capacitive deionization, Next Mater. 9 (2025) 100953.
[98] G. Bhaskaran, et al., Layered hydrated-titanium-oxide-laden reduced graphene oxide composite as a high-performance negative electrode for selective extraction of Li via membrane capacitive deionization, J. Colloid Interface Sci. 650 (2023) 752–763.
[99] B. Hu, et al., Go-encapsulated La-doped lithium manganese oxide assemblies to enhance lithium extraction performance in capacitive deionization, Sep. Purif. Technol. 348 (2024) 127693.
[100] J. Si, et al., Selective membrane capacitive deionization for superior lithium recovery, Desalination 572 (2024) 117154.
[101] A. Siekierka, B. Tomaszewska, M. Bryjak, Lithium capturing from geothermal water by hybrid capacitive deionization, Desalination 436 (2018) 8–14.
[102] J. Hu, et al., Enhanced Interfacial charge transport of Ni metal–organic framework nanosheets interconnected by carbon nanotubes for capacitive deionization, ACS Appl. Nano Mater. 7 (17) (2024) 19981–19990.
[103] L. Wan, et al., In situ construction of rod-shaped Fe3O4/N-doped carbon architecture with superior lithium-ion extraction performance via employing hybrid capacitive deionization system, Desalination 601 (2025) 118538.
[104] Y. Xu, et al., LiMn2O4 nanoparticles in situ embedded in carbon networks for lithium extraction from brine via hybrid capacitive deionization, ACS Appl. Mater. Interfaces 17 (3) (2025) 4821–4831.
[105] G.Q. Ma, et al., Binder-free LiMn2O4 nanosheets on carbon cloth for selective lithium extraction from brine via capacitive deionization, Small 20 (9) (2024).
[106] J. Li, et al., Lithium extraction via capacitive deionization: AlF3 coated LiMn2O4 spheres for enhanced performance, Desalination 591 (2024) 118035.
[107] N. Xie, et al., Fabricating a flow-through hybrid capacitive deionization cell for selective recovery of lithium ions, ACS Appl. Energy Mater. 4 (11) (2021) 13036–13043.
[108] H. Joo, et al., Application of a flow-type electrochemical lithium recovery system with λ-MnO2/LiMn2O4: experiment and simulation, ACS Sustain. Chem. Eng. 8 (26) (2020) 9622–9631.
[109] J. Yang, et al., In situ growth of LiMn2O4 on graphene oxide for efficient lithium extraction by capacitive deionization, J. Solid State Electrochem. 27 (8) (2023) 2029–2037.
[110] T. Elmakki, et al., Capacitive lithium capture system using a mixed LiMn2O4 and LiAlO2 material, Desalination 593 (2025) 118195.
[111] J. Zhou, et al., Breaking the trade-off between capacity, stability, and selectivity for electrochemical lithium extraction via a dual-ion doping strategy, Desalination 600 (2025) 118530.
[112] Q. Jiang, X. Zhang, J. You, SnO(2): a wonderful electron transport layer for perovskite solar cells, Small 14 (31) (August 2, 2018) 1801154.

[113] W.-J. Yu, et al., Incorporation of SnSe2/SnO2 heterostructures in carbon nanotubes for excellent lithium storage performance, J. Alloys Compd. 1010 (2025) 177273.
[114] C. Lin, et al., Dual carbon confining SnO2 nanocrystals as high-performance anode for sodium-ion batteries, J. Power Sources 623 (2024) 235426.
[115] J. Lao, et al., Aqueous stable Ti3C2 MXene membrane with fast and photoswitchable nanofluidic transport, ACS Nano 12 (12) (2018) 12464–12471.
[116] D. Er, et al., Ti3C2 MXene as a high capacity electrode material for metal (Li, Na, K, Ca) ion batteries, ACS Appl. Mater. Interfaces 6 (14) (2014) 11173–11179.
[117] Z. Li, et al., Intercalation-deintercalation design in MXenes for high-performance supercapacitors, Nano Res. 15 (4) (2022) 3213–3221.